Morphology- and size-controlled synthesis of a metal-organic framework under ultrasound irradiation: an efficient carrier for pH responsive release of anti-cancer drugs and their applicability for adsorption of amoxicillin from aqueous solution

Reza Abazari, Ali reza Mahjoub, Alexandra M.Z. Slawin, Cameron L. Carpenter-Warren

PII: S1350-4177(17)30603-X
DOI: https://doi.org/10.1016/j.ultsonch.2017.12.032
Reference: ULTSON 4016

To appear in: *Ultrasonics Sonochemistry*

Received Date: 28 October 2017
Revised Date: 15 December 2017
Accepted Date: 15 December 2017

Please cite this article as: R. Abazari, A. reza Mahjoub, A.M.Z. Slawin, C.L. Carpenter-Warren, Morphology- and size-controlled synthesis of a metal-organic framework under ultrasound irradiation: an efficient carrier for pH responsive release of anti-cancer drugs and their applicability for adsorption of amoxicillin from aqueous solution, *Ultrasonics Sonochemistry* (2017), doi: https://doi.org/10.1016/j.ultsonch.2017.12.032

Morphology- and size-controlled synthesis of a metal-organic framework under ultrasound irradiation: an efficient carrier for pH responsive release of anti-cancer drugs and their applicability for adsorption of amoxicillin from aqueous solution

Reza Abazari,[a] Ali reza Mahjoub,[*,a] Alexandra M. Z. Slawin,[b] and Cameron L. Carpenter-Warren[b]

[a]*Department of Chemistry, Tarbiat Modares University, P.O. Box 14115-175, Tehran, Iran*

[b]*EaStCHEM, School of Chemistry, University of St Andrews, St Andrews, Fife, KY16 9ST, Scotland, UK*

---

* Tel.: +98 2182883442; fax. +98 2182883455. E-mail address: r.abazari@modares.ac.ir (R. Abazari); mahjouba@modares.ac.ir (A. R. Mahjoub).

Abstract

In this study, we have reported a biocompatible metal-organic framework (MOF) with ultra-high surface area, which we have shown to have uses as both a cancer treatment delivery system and for environmental applications. Using a sonochemical approach, highly flexible organic H_3BTCTB and ditopic 4,4´-BPDC ligands, along with modulators of acetic acid and pyridine were combined to prepare a Zn(II)-based metal-organic framework, DUT-32, $[Zn_4O(BPDC)(BTCTB)_{4/3}(DEF)_{39.7}(H_2O)_{11.3}]$. Powder X-ray diffraction (PXRD), field-emission scanning electron microscopy (FE-SEM), and Fourier transform infrared spectroscopy (FTIR) were used to characterize, the particle size, shape, and structure of the DUT-32. To show the effects of shape and size of DUT-32 micro/nano-structures on doxorubicin (DOX) drug release and amoxicillin (AMX) adsorption, time of sonication, initial reagent concentrations, irradiation frequency, and acetic acid to pyridine molar ratios were optimized. The drug-loaded DUT-32 was soaked in simulated body fluid (SBF) and the drug release ratio was monitored through release time to perform *in vitro* drug release test. A slow and sustained release was observed for DUT-32 micro/nano-structures, having a considerable drug loading capacity. At the pH values 7.4-4.5, various profiles of pH-responsive release were achieved. Also, the prepared DUT-32 micro/nano-structures are found to be biocompatible with PC3 (prostate cancer) and HeLa (cervical cancer) cell lines, when tested by MTT assay. Moreover, DUT-32 micro/nano-structures were studied to show AMX adsorption from aqueous solution. Finally, kinetic studies indicated that AMX adsorption and drug release of DOX via this MOF are of first-order kinetics.

Keywords: *Metal-organic framework, Modulator, Drug delivery, pH responsive release, Doxorubicin, Amoxicillin.*

1. Introduction

As a result of their poor solubility, numerous side effects and non-specificity, many anticancer drugs have poor efficiency when it comes to treating the target tumor and often end up severely damaging healthy cells throughout the body [1-4]. Therefore, special attention has been paid to nano-carriers for drug delivery anticancer therapy, aiming at a targeted release of anticancer drugs while keeping the adjacent healthy cells unaffected [5-8]. In this context, porous materials have proved to be very successful for drug delivery, possessing advantages such as: high pore volume, considerable surface area, and size-adjustable pores [9-14]. Nevertheless, it is a great challenge to prepare porous materials in a way that their pore shape and size can be controlled [15-17].

From a biomedical perspective, drug release from porous materials is performed in reaction to the body's pH level. This reliance of the drug delivery system on the pH value in the body allows for a proper targeted drug delivery, owing to the inhibition of drug release during systemic circulation at a physiological pH of 7.4, and hence the drug is only released as it encounters the cancerous cells' acidic environment, leaving neighboring healthy cells unharmed [18-20]. Therefore, a proper physiological stimulus for pH-responsive drug delivery can be provided by the pH variations in various tissues, organs, and cell parts [21, 22]. As an example, compared to the normal tissue and blood, tumorous extracellular microenvironments (pH = 5.7–7.8), lysosome (pH = 4.5–5.0) and endosome (pH = 5.5–6.0) compartments are more acidic [23-25].

Recently, medical pollutants (e.g., pollutants caused by the pharmaceutical and personal care products) have adversely affected different aqueous media such as groundwater, surficial water, wastewater, and even drinking water [26]. In this context, antibiotic organics have attracted much attention since they are highly toxic and cannot be easily filtered through sewage filtration

equipment and thus threaten the environment [27, 28]. When accumulated in the body, these antibiotics can damage the central nervous system, joints, kidneys, etc. [29]. In this study, a lactam antibiotic, amoxicillin (AMX), which is common in the treatment of both humans and animals, is considered. If 500 mg of AMX is orally administered in humans, then 86 ± 8% excretion in the urine is observed in 2 h of consumption since AMX has a slow metabolism rate in humans [30-32]. Despite the sensitivity of AMX towards hydrolysis in different pH values [33], complete degradation of AMX is difficult as its different hydrolyzed and metabolized by-products remain present in both urine and feces. Nevertheless, this antibiotic is indigestible, and hence it is metabolically dischargeable. AMX is present in both surficial water and secondary water drainage at μg L^{-1} concentrations [34-37]. As a result of its chemical stability, low rate of biodegradation and high biological toxicity, it is imperative that research be conducted into removal of this persistent organic pollutant (POP) from our water systems.

Owing to their significant chemical and physical characteristics (such as record internal surface areas, tunable pore size and seemingly limitless functionalisability), metal-organic frameworks (MOFs), sometimes referred to as porous coordination polymers (PCPs), have been in the focus of scholarly attention worldwide [38-40]. MOFs can consist of a wide range of inorganic metal nodes and organic linkers, that serve as hosts for numerous guest molecules, meaning that there is seemingly infinite scope for the morphology and chemical functionality of the pores and internal surfaces to be systematically tuned and improved [41]. This high degree of tunability results in several advantages when it comes to drug loading: It means that theoretically a MOF can be developed with the perfect pore size, functionality and guest interactions to both hold and release the drug of interest. In addition, MOFs very high specific surface area gives them the ability to absorb high quantities of guest molecules [42-46]. Application of nano-MOFs for drug

delivery was first proposed by G. Ferey and W.B Lin and other teams [47-50]. As recorded in the literature, the MOFs react to the changes of pH, where they can store and release drugs by a mechanism of forming and cleaving the coordination bonds, respectively [51]. On the other hand, MOFs are outstanding absorption substances since they are very porous and their specific surface area is large.

The ratio of surface area to volume in nanomaterials is much greater than that of larger particles. Thanks to novel synthesis approaches which control the size and morphology of micro/nanostructures, the nanostructured coordination compounds such as nano metal-organic frameworks have recently been enhanced [52]. Much attention has been paid to the reduction of MOF size to micro and nano [53-55]. Different approaches have already been suggested for nano-scaled synthesis of MOFs with specific shape [56-58]. Synthetic approaches involving ultrasound offer several advantages, including: speed, ease, low cost, ecofriendly and control over size and shape of the particles. In sonochemistry, the generating, growing, and collapsing of bubbles or 'acoustic cavitation' are needed. Somehow this works, is that local hot spots are formed which generate high pressures, up to 1000 atm, and temperatures up to 5000 ℃ having brief lifetime. As a result of these extraordinary physical characteristics, the synthesis of the nanostructures might be furthered, especially through the growth in the crystallization nucleuses [59, 60]. To do so, the ultrasonic illumination takes advantage of the acoustic cavitation comprising the bubble formation, growth, and implosive collapse in an aqueous solution. One protocol for controlling the size and the morphology of MOFs is modulating synthesis. The crystal growth can be directed towards desirable particle shape and size if sonochemistry is combined with modulating synthesis [61-66].

Using sonochemistry, the present study has sought to optimize the shape and the size of the nanostructured DUT-32 particles by varying the ultrasound illumination time and initial reagent

concentration in vicinity of the modulator. Also, the particles size and shape effects on the MOFs capacity for drug adsorption and drug delivery have been explored. DUT-32 shows excellent biocompatibility with two different cell lines. To the best of the authors' knowledge, this is the first attempt to investigate DUT-32 nanostructures for AMX adsorption and drug release of DOX (Scheme 1). Our results can be used as a starting point for further investigation of other applications, such as the environmental remediation for determinate rule shape and the size the nanostructured MOFs for higher efficiency.

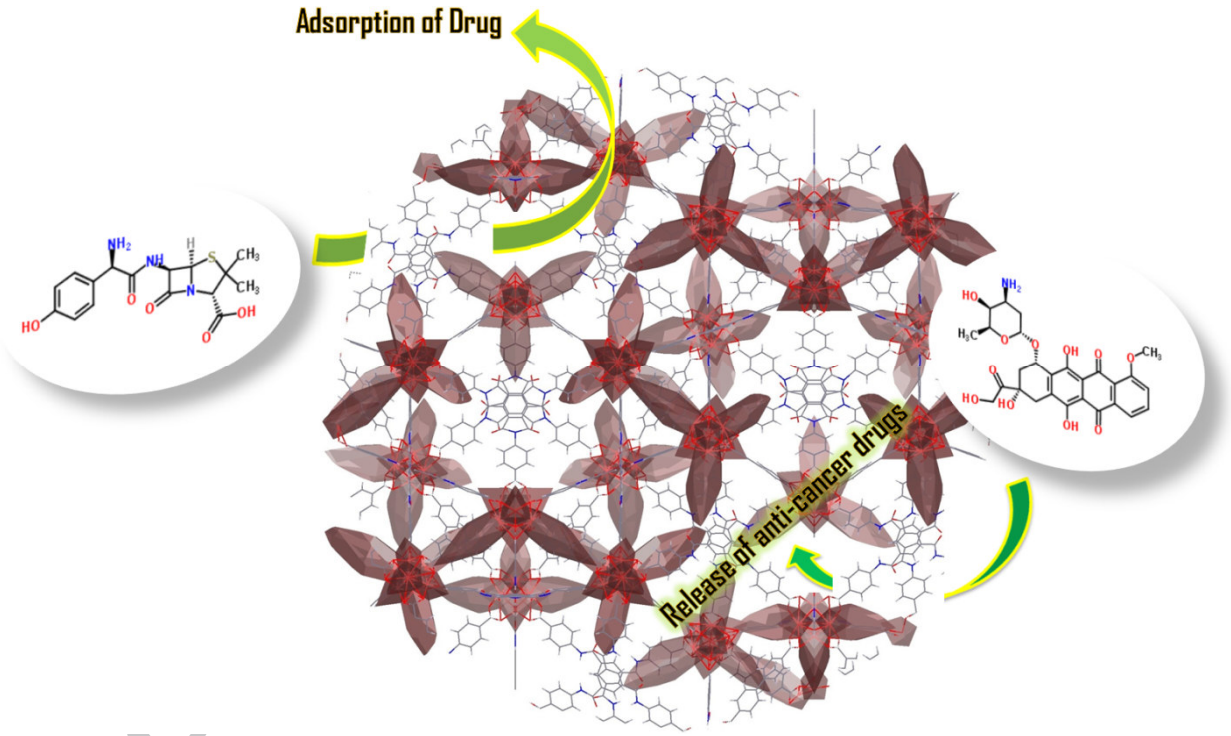

Scheme 1. Schematic showing DUT-32 absorbing AMX and releasing DOX.

2. Experimental

2.1. Materials and physical techniques

All reagents for the synthesis and analysis were commercially available from Merck and Sigma-Aldrich Companies and used as received. The following chemicals were used in the synthesis

procedure: Zinc(II) acetate dihydrate ($Zn(CH_3COO)_2.2H_2O$ 98%, Merck), Zinc nitrate hexahydrate ($Zn(NO_3)_2.6H_2O$ 98%, Sigma-Aldrich), and N,N Diethylformamide (DEF 99%, Sigma-Aldrich). Water used in the experiments was deionized (DI) and doubly distilled prior to use as a washing agent. The ligands of 4,4´-biphenyldicarboxylic acid (4,4´-BPDC) and 4,4´,4´´-[1,3,5-benzenetriyltris(carbonylimino)]trisbenzoic acid (H_3BTCTB) were prepared by the reported methods [67, 68].

The shape (or surface morphology), size, and crystal structure of the DUT-32 micro/nano-structures were characterized by field emission scanning electron microscopy (FE–SEM), Powder X–ray diffraction (PXRD), UV–Visible absorption spectroscopy, and Fourier transform infrared spectroscopy (FTIR). A Hitachi S–1460 field emission scanning electron microscope at an accelerating voltage of 15 kV was employed to obtain the FE–SEM images. For all of the samples, PXRD analyses was performed using a Philips diffractometer (Model TM–1800), using a nickel filtered Cu–Kα radiation source (λ = 1.542 Å). It uses a proportional counter detector at a 4°/min scan rate, with a scanning angle of 2θ=1°-50° with a 40-kV voltage and a potential current of 30 mA. For all samples, the measurement of the UV–Vis absorption spectra was carried out in a quartz cell using a Camspec M330 UV–Vis spectrometer (200–700 nm). The FTIR spectra (in 400-4000 cm^{-1} wavenumbers) were obtained using KBr disks on a Shimadzu FTIR model Prestige 21 spectrometer. Ultrasonic generation was carried out in an ultrasonic bath SONICA-2200 EP (frequency of 40 kHz).

2.2. Solvothermal synthesis of DUT-32 crystals

Single crystals of *DUT-32* were prepared according to the previously reported solvothermal procedure [68].

2.3. Synthesis of DUT-32 micro/nano-structures

Using various metal and ligands concentrations, DUT-32 micro/nano-structures were synthesized at ambient temperature and atmospheric pressure via irradiation in an ultrasonic bath for 30, 60, 90, and 120 minutes (Table 1). The products were then separated by centrifuge, washed with DEF and then dried in air.

Table 1. Experimental details for synthesis of DUT-32 micro/nano-structures.

Samples name	Time (min)	Molar ratio (H_3BTCTB: 4,4´-BPDC: $Zn(CH_3COO)_2.2H_2O$ mmol) in 20 ml DEF	Concentration [H_3BTCTB]/[4,4´-BPDC]/[$Zn(CH_3COO)_2.2H_2O$] (M)	Frequency	Modulator (3 ml)	Morphology
DUT-32-A	30	0.1:0.125:0.5	[0.005]/[0.006]/[0.025]	40	-	Non-uniform particles
DUT-32-B	60	0.1:0.125:0.5	[0.005]/[0.006]/[0.025]	40	-	particles
DUT-32-C	90	0.1:0.125:0.5	[0.005]/[0.006]/[0.025]	40	-	Non-uniform micro/nano-structures
DUT-32-D	120	0.1:0.125:0.5	[0.005]/[0.006]/[0.025]	40	-	Agglomerate structures
DUT-32-E	60	0.3:0.125:0.5	[0.015]/[0.006]/[0.025]	40	-	Agglomerate structures
DUT-32-F	60	0.1:0.375:0.5	[0.005]/[0.018]/[0.025]	40	-	Non-uniform needle
DUT-32-G	60	0.3:0.375:0.5	[0.015]/[0.018]/[0.025]	40	-	Non-uniform micro/nano-structures
DUT-32-H	60	0.3:0.375:1.5	[0.015]/[0.018]/[0.075]	40	-	Agglomerate structures
DUT-32-I	60	0.1:0.125:0.5	[0.005]/[0.006]/[0.025]	30	-	Non-uniform micro/nano-structures
DUT-32-J	60	0.1:0.125:0.5	[0.005]/[0.006]/[0.025]	60	-	Layer by layer
DUT-32-K	60	0.1:0.125:0.5	[0.005]/[0.006]/[0.025]	40	Pyridine	Plates
DUT-32-L	60	0.1:0.125:0.5	[0.005]/[0.006]/[0.025]	40	Acetic acid	Spindles
DUT-32-M	60	0.1:0.125:0.5	[0.005]/[0.006]/[0.025]	40	Acetic acid + Pyridine	Non-uniform plates

2.4. Drug loading and in vitro drug release

The loaded samples adsorption with DOX was measured to estimate the amount of drug which can be loaded into the DUT-32 structure. The sample was dissolved in DMSO and spectrophotometry at 482 nm was performed. For determination of the drug concentration in solution, a calibration curve of free DOX content was established. The formulae below were used to obtain the drug loading content (DLC) and drug loading efficiency (DLE), (Eqs. 1 and 2).

$$Drug\ Loading\ Content\ (DLC) = \left[\frac{\text{amount of DOX in carrier}}{\text{amount of DOX– loaded carriers}}\right] \times 100\% \qquad (Eq.1)$$

$$\text{Drug Loading Efficiency (DLE)} = \left[\frac{\text{amount of DOX in carrier}}{\text{amount of DOX for carrier preparation}}\right] \times 100\% \ (Eq.2)$$

In order to perform the release test *in vitro*, under atmospheric pressure, the DOX-loaded DUT-32-K was compacted into a disk (0.12 g, d = 7 mm), which was sealed into a dialysis bag (molecular cut off 50 kD). Under constant shaking, it was soaked in 200 mL of phosphate buffer solution (SBF at pHs equal to 7.4, 6, and 4.5) at 37 ℃. Then, in order to perform UV–Vis analysis, the doxorubicin-release medium was extracted at pre-determined time intervals. Finally, it was substituted with fresh SBF.

2.5. Cell lines and in vitro toxicological study

In this work two cell lines, prostate cancer cell line (PC3) and cervical cancer cell line (HeLa), were selected and investigated to characterize the biocompatibility of the DUT-32-K micro/nano-structures as drug delivery systems in a test for *in vitro* toxicity. PC3 cell was cultured in RPMI-1640 medium supplemented with 10% (v/v) fetal bovine serum (FBS) and 1%

(v/v) penicillin/streptomycin solution at 37 ℃ under a humidified atmosphere of 5% CO_2. HeLa cells were cultured in Dulbecco's modified Eagle's medium (DMEM) supplemented with 10% (v/v) FBS and 1% (v/v) penicillin/streptomycin solution at 37 ℃ under a humidified atmosphere of 5% CO_2. In order to examine the toxicity of the DUT-32-K micro/nano-structures, eight different concentrations were used and an MTT [3-(4,5-dimethylthiazol-2- yl)-2,5-diphenyltetrazolium bromide] assay was carried out on the cell lines of PC3 and HeLa., Seeding of the cells in 96 well plates was performed at a density of 5100 per well, where the cells were left to adhere for 24 h. For 72 h, these cells were then incubated at eight different concentrations of DUT-32-K. After that, in a media with 0.5 mg mL^{-1} of MTT, the incubation was done at 37 ℃ for 3–4 h. In a MTT solubilizing buffer, the produced formazan crystals were dissolved. Using a microplate reader, the absorbance was calculated at 570 nm, and then a comparison was made between these values and those of the control cells. Meanwhile eight different concentrations of free DOX and DOX/DUT-32-K were used against PC3 and HeLa cells using the above mentioned procedure.

2.6. Adsorption Equilibrium Studies

1 mg of adsorbent was used for each 50 ml of AMX solution (20 ppm) under stirring so that the assays of adsorption were carried out. Solid phase filtration was performed at defined intervals using centrifugation. UV–Vis spectroscopy was used to calculate the concentration of AMX remaining in the solution, Eq. 3 is used to allow calculation of the DUT-32-K absorption capacity. In order to determine the adsorption capacity, while the removal efficiency can be calculated by Eq. 4.

$$Adsorption\ capacity = \frac{(C_0 - C_e)V}{m} \qquad (Eq.3)$$

$$\%Removal\ efficiency = \frac{C_0 - C_e}{C_0} * 100 \qquad (Eq. 4)$$

Here, the initial and equilibrium liquid phase concentrations of AMX are given by C_o (mg. L^{-1}) and Ce (mg. L^{-1}) respectively. Also, the total solution volume is shown by V(L), and m (g) stands for the adsorbent mass.

3. Results and discussion

Morphology and size-controlled synthesis via sonochemical methods has already been used for a rapid and simple synthesis of DUT-32, $C_{54}H_{32}O_{17}N_4Zn_4{\times}39.7\ C_5H_{11}NO{\times}11.3\ H_2O$ $[Zn_4O(BPDC)(BTCTB)_{4/3}(DEF)_{39.7}(H_2O)_{11.3}]$ on large scales. Using two symmetry-independent Zn_4O^{6+} octahedral secondary building units, the DUT-32 structure is formed. These two units are coordinated to two $BPDC^{2-}$ and four $BTCTB^{3-}$ linkers. Ditopic ligands of $BPDC^{2-}$ have been set in a trans orientation in the first Zn_4O^{6+} cluster; however, in the second cluster the linkers have a cis orientation in terms of one another. These links create a three-dimensional framework, in which three dissimilar but large mesopores (30 × 40 Å, 28 × 32 Å and 20 × 26 Å, assuming van der Waals radiuses of the atoms) as well as one smaller micropore (14 × 18 Å) can be observed (Figs. 1-3). There are two independent Zn/O inorganic clusters in the structure: The first lies on a general position and involves Zn1-Zn4 and O1, whereas the second cluster involves Zn5-Zn7 and O2 and has a mirror plane running through Zn5, Zn7 and O2. The $BPDC^{2-}$ linkers join these two different inorganic clusters and possess an inversion center on the C5-C5 bond. There are two crystallographically independent environments for the $BTCTB^{3-}$ linkers: The first is coplanar with the same mirror which runs through the second inorganic cluster and has a 3-fold axis running normal to the center ring. The second $BTCTB^{3-}$ linker is intersected by the same mirror

plane, however this time it is normal to the plane of the linker, running through C79, C80, C83 and N7.

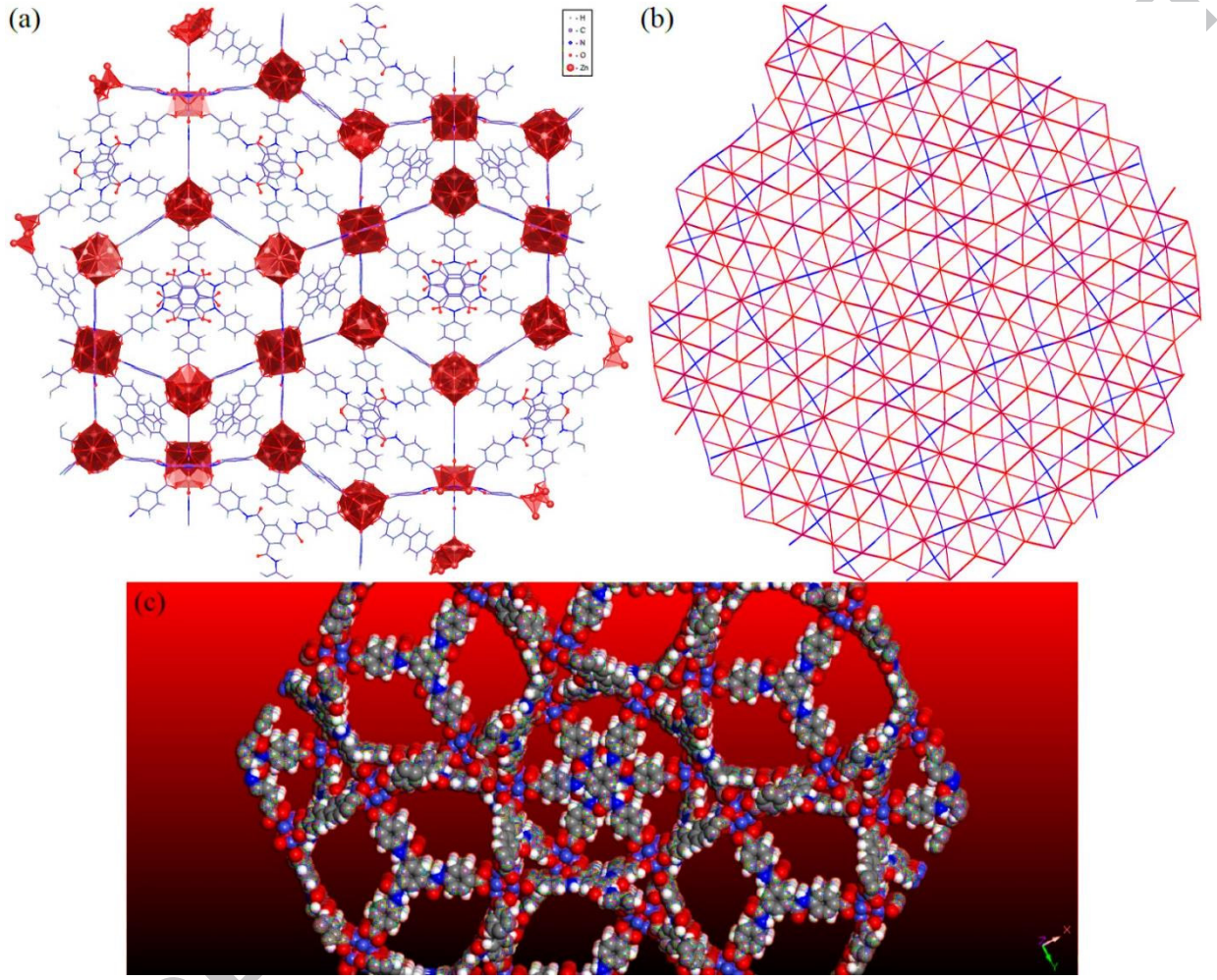

Fig. 1. (a) 3D extended structure of DUT-32, viewed down the *b* axis and with the Zn/O inorganic clusters drawn as polyhedrons, (b) a 3D simplified net of DUT-32 looking down the *b* axis, with pink as the metal centers, red as the $BTCTB^{3-}$ linkers and blue for the $BPDC^{2-}$ linkers, and (c) space-filling view of DUT-32 structure as viewed along a axis to show three-dimensional structure. All disordered guest molecules are omitted for clarity.

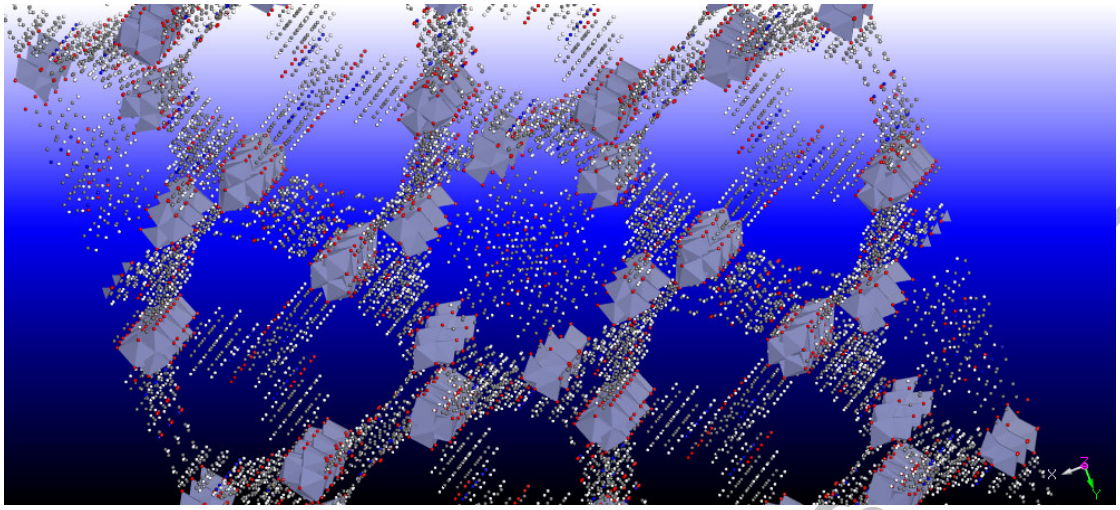

Fig. 2. Polyhedral representation of DUT-32 structure as viewed along the z axis to show three-dimensional structure.

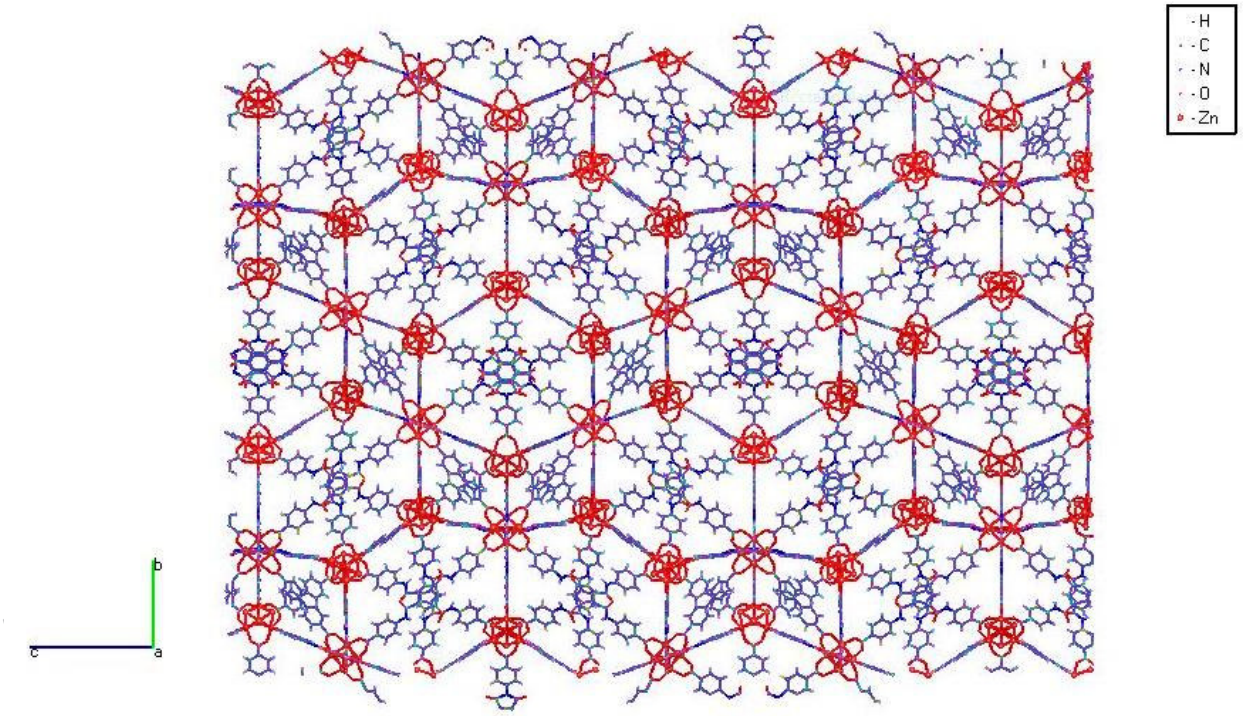

Fig. 3. Perspective view of DUT-32 structure as viewed along the a axis to show three-dimensional structure.

The solvothermal reaction of $Zn(NO_3)_2.6H_2O$ with H_3BTCTB and the 4,4´-BPDC carboxylate ligand in the molar ratio of 5:1:1.25 at 100 ℃ and for 48 h, yielded white crystals of the DUT-32. On the other hand, under the ultrasonic illumination, micro/nano-structures of the DUT-32 compound were achieved in the DEF solvent at ambient temperature in the minutes-hours timescale. Two different synthesis routes for the preparation of $[Zn_4O(BPDC)(BTCTB)_{4/3}(DEF)_{39.7}(H_2O)_{11.3}]$ are described in Fig. 4.

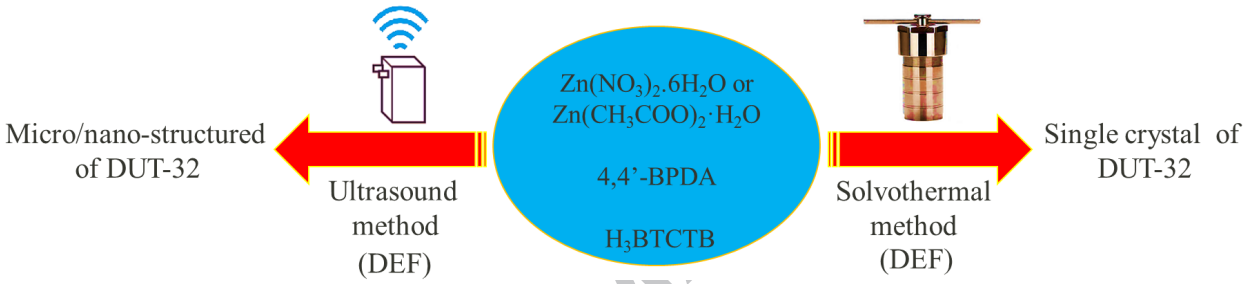

Fig. 4. Schematic showing the synthetic routes to both single crystals and micro/nanostructured DUT-32.

3.1.Sonication time

In the first step, viewed by field emission scanning electron microscopy (FE-SEM), the size and the shape of the sonochemically-synthesized DUT-32 micro/nano-structures were characterized by varying four parameters, namely: The time of sonication, initial reagent concentration, irradiation intensity, and help from modulators – as shown in Figs. 5 to 8. The preparation was carried out at four different sonication durations (samples of DUT-32-A to DUT-32-D) so as to explore the impacts of the time of sonication on DUT32 micro/nano-structures size and morphology. In this context, the optimal value of the sonication time was observed to be 60 min when the DUT-32-B nanostructures show increased regularity and uniformity in their size and

morphology (Fig. 5b). As the time of sonication was increased to 90 min and particularly when it was increased to 120 min (DUT-32-C and DUT-32-D), uniformity of the structures diminished and agglomerated forms were observed (Figs. 5c and d). When the time of sonication was reduced to 30 minutes (DUT-32-A), dissimilar sizes and irregular structures were resulted (DUT-32-A). Therefore, the optimal time of sonication was considered to be 60 min, and the other factors influencing the DUT-32 micro/nano-structures final morphology were scrutinized.

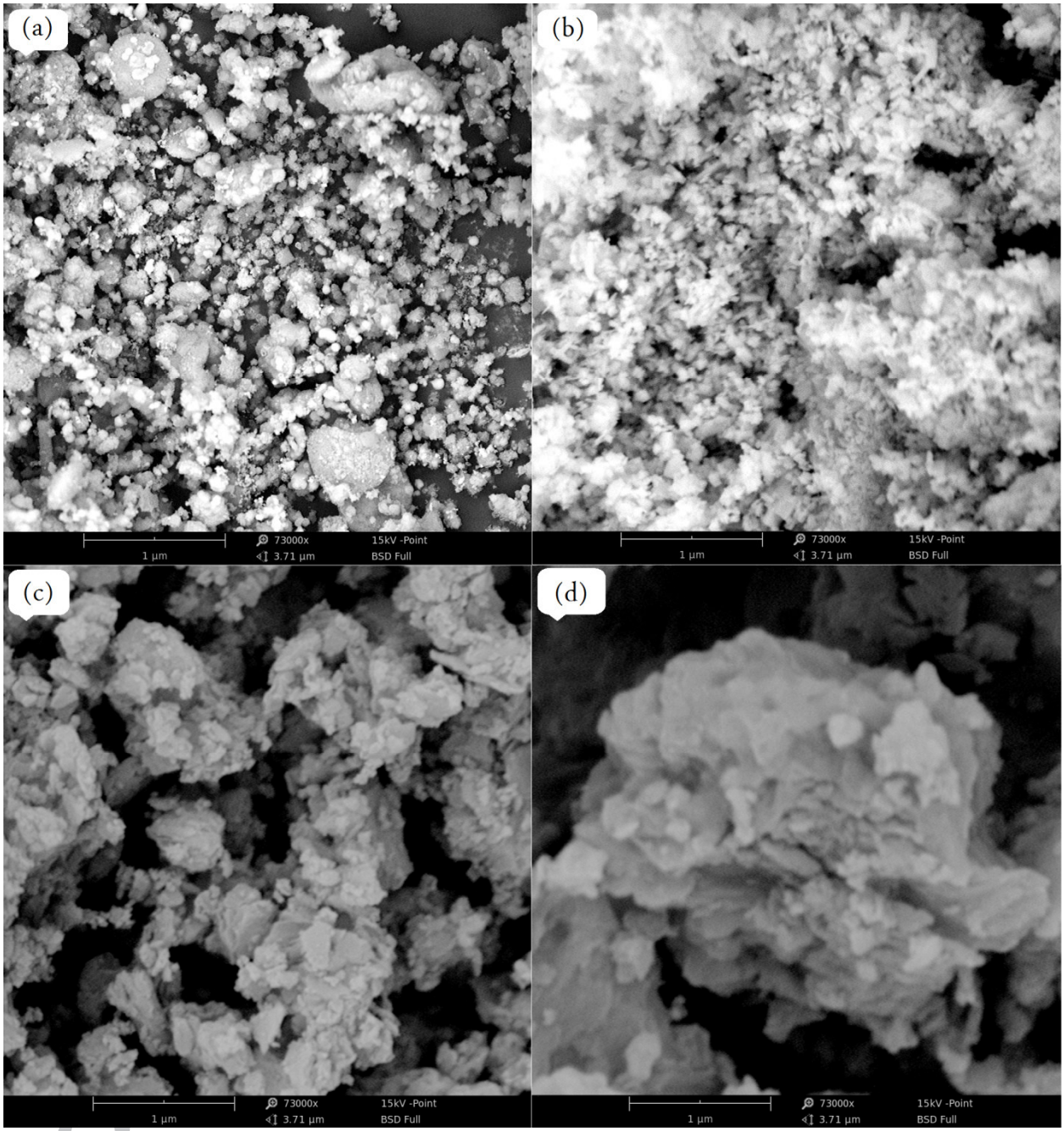

Fig. 5. FE-SEM images of DUT-32 micro/nano-structures prepared through the sonochemical reaction with fixed reagent concentrations and fixed irradiation frequency in the absence of modulators at various times of sonication a) 30 min, b) 60 min, c) 90 min, and d) 120 min.

3.2. Concentration of starting materials

The aforesaid procedures were carried out with different reagent concentrations so that the impact of the initial reagent concentration on the nanostructured DUT-32 particle shape and size could be investigated (Fig. 6 a-d). To this end, four other experiments (DUT-32-E to DUT-32-H samples) were carried out. It was observed that the higher the concentration of the reagents, the less regular the shape of the resultant nanostructures and greater their mean diameter (Fig. 4). At lower reagent concentrations, the particles are more spherical, whereas at higher concentrations they adopt plate formations. However, in order to reduce the costs of the used materials and due to the importance of the nanostructure compounds, as already suggested in the introduction section, the lower initial concentrations were selected and studied as the optimal concentrations. In other words, the initial materials concentrations for DUT-32-B sample are here regarded as the optimum value. It was also found that the effect of increased concentration of the original reagents on the morphology and size of the said compounds are quite similar to the sonication time effect. In that there is an optimum value ([0.3:0.125:0.5]) where particle shape and size is uniform, but higher concentrations result in particle agglomeration. Also, it was observed that with the increased concentration and a longer time of reaction, the nanoparticles became agglomerated. Our obtained results were in close agreement with those in the literature [69]. It can be accounted for by the fact that nuclei growth is hindered by a rapid kinetics. Centers of nucleation are created in the bubbles and these centers have a limited growth due to the short collapse [70].

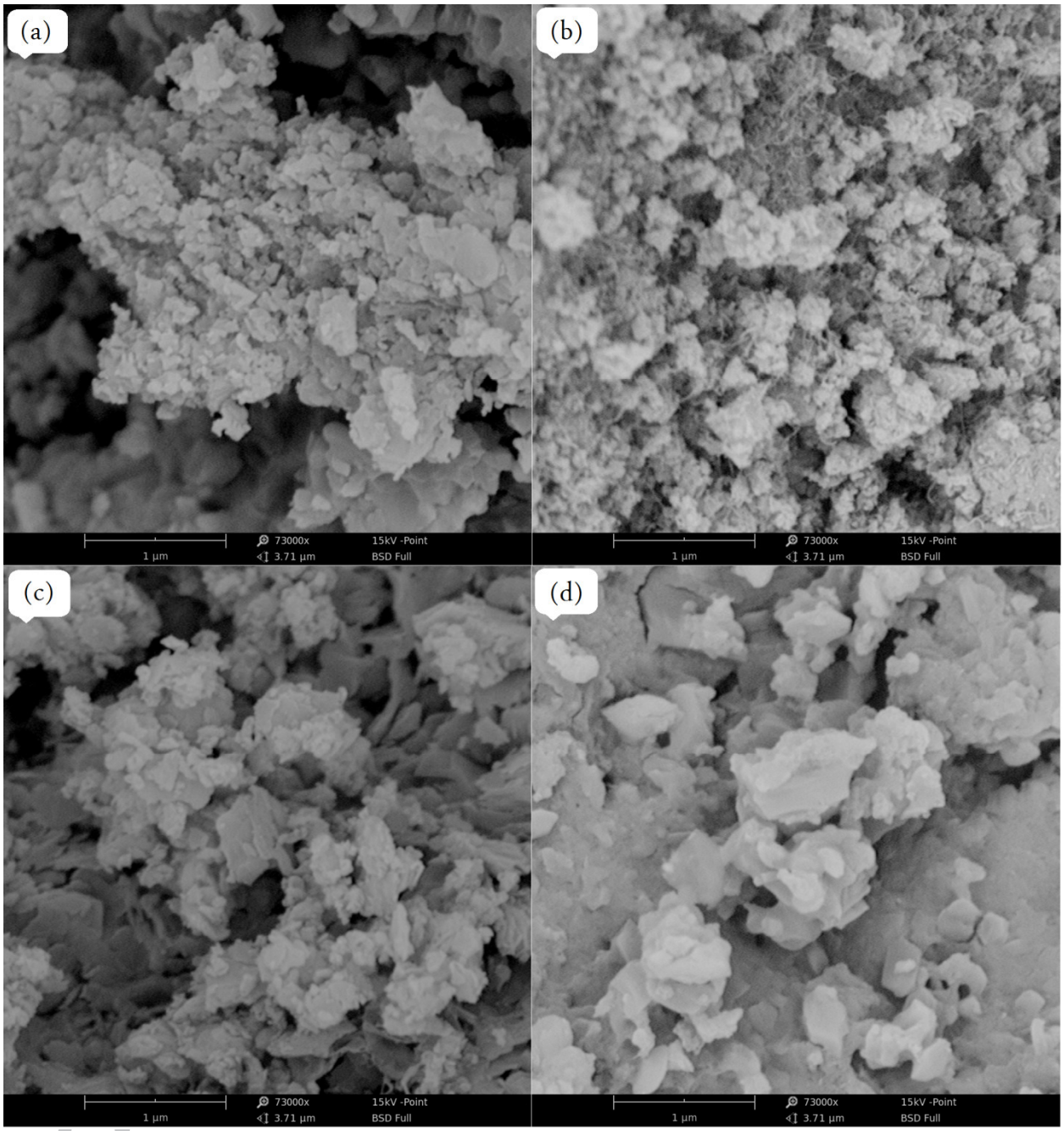

Fig. 6. FE-SEM images of DUT-32 micro/nano-structures prepared by sonochemistry method having a 60-min sonication time under various molar ratios of the reagents [H_3BTCTB:4,4´-BPDC:$Zn(CH_3COO)_2.2H_2O$]: a) [0.3:0.125:0.5], b) [0.1:0.375:0.5], c) [0.3:0.375:0.5], and d) [0.3:0.375:1.5].

3.3. Effect of irradiation frequency

The irradiation time for DUT-32-I and DUT-32-J samples were fixed at 60 minutes, with fixed reagent concentration. DUT-32-I, irradiation frequency of 30 kHz, the plate-like structures agglomeration decreased, and size distribution was wider from nano to micro scales (for DUT-32-B sample, however, the irradiation frequency increased to 40 kHz). Furthermore, when DUT-32 irradiation frequency became greater (60 kHz for sample of DUT-32-J) than those of DUT-32-I and DUT-32-B samples, an increase occurred in the nanostructures size and agglomeration (Fig. 7b).

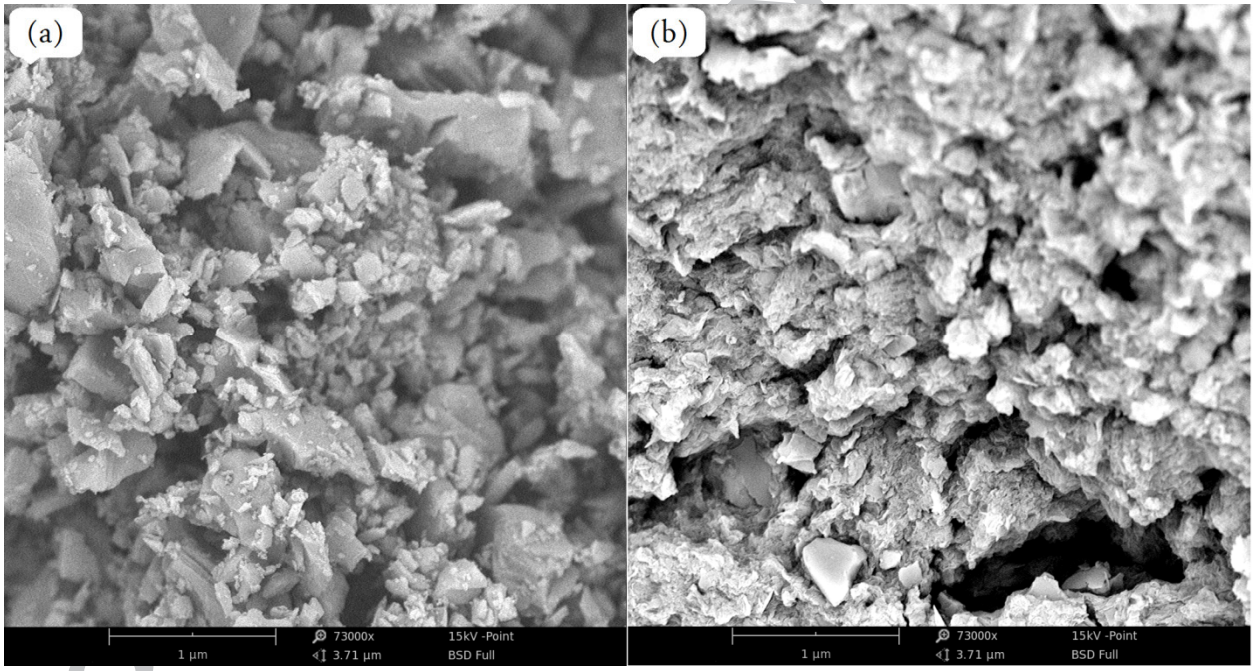

Fig. 7. FE-SEM images of DUT-32 micro/nano-structures produced by sonochemical process at fixed reagents concentrations with a 60-min time of sonication having different two irradiation intensities a) 30 kHz and b) 60 kHz.

3.4. Effect of pyridine and acetic acid as modulator reagents

In this work, ultrasonic irradiation has been coupled with the modulation method. The coordination equilibriums have been modulated using the ultrasound irradiation just by the addition of the pyridine an acetate ion modulators. These modulators have a chemical functionality similar to that of the linkers. When modulator reagents are employed, the coordination interaction between the organic linkers and the metal ions is inhibited, hence a competitive situation is created in which the crystal growth and framework extension rate is regulated. Samples DUT-32-K to DUT-32-M were synthesized under fixed reagent concentrations (0.1:0.125:0.5 molar ratios of H_3BTCTB:4,4´-BPDC:$Zn(CH_3COO)_2.2H_2O$ respectively), irradiation frequency (40 kHz) and duration (60 minutes), and modulator volume (3ml). The type of modulator used in the syntheses was varied across samples DUT-32-K to DUT-32-M, using pyridine, acetic acid, and a 50:50, v:v mixture respectively. From looking at the FE-SEM images (Fig. 8), it was found that pyridine produced the particles with the most uniform size and shape, followed by acetic acid, and finally the mixture which gave much larger non-uniform particles. In other words, results showed that although the main morphology has not changed, the presence of pure pyridine has led to the synthesis of the new plate-like morphologies in DUT-32-K sample. Under close scrutiny, the particles produced by the pyridine modulator show new plate-like morphologies, along with directional growth and smaller thicknesses. In this context, we have made use of our three synthesized samples (i.e. DUT-32-B, DUT-32-K, and DUT-32-L micro/nano-structures) as models in our applications so that better results can be provided under these optimized conditions. It can be concluded therefore, that the size and morphology of the MOF nanostructure is dependent on all four synthetic variables that we investigated, highlighting that it is important to optimize these conditions when synthesizing any new MOF via this method.

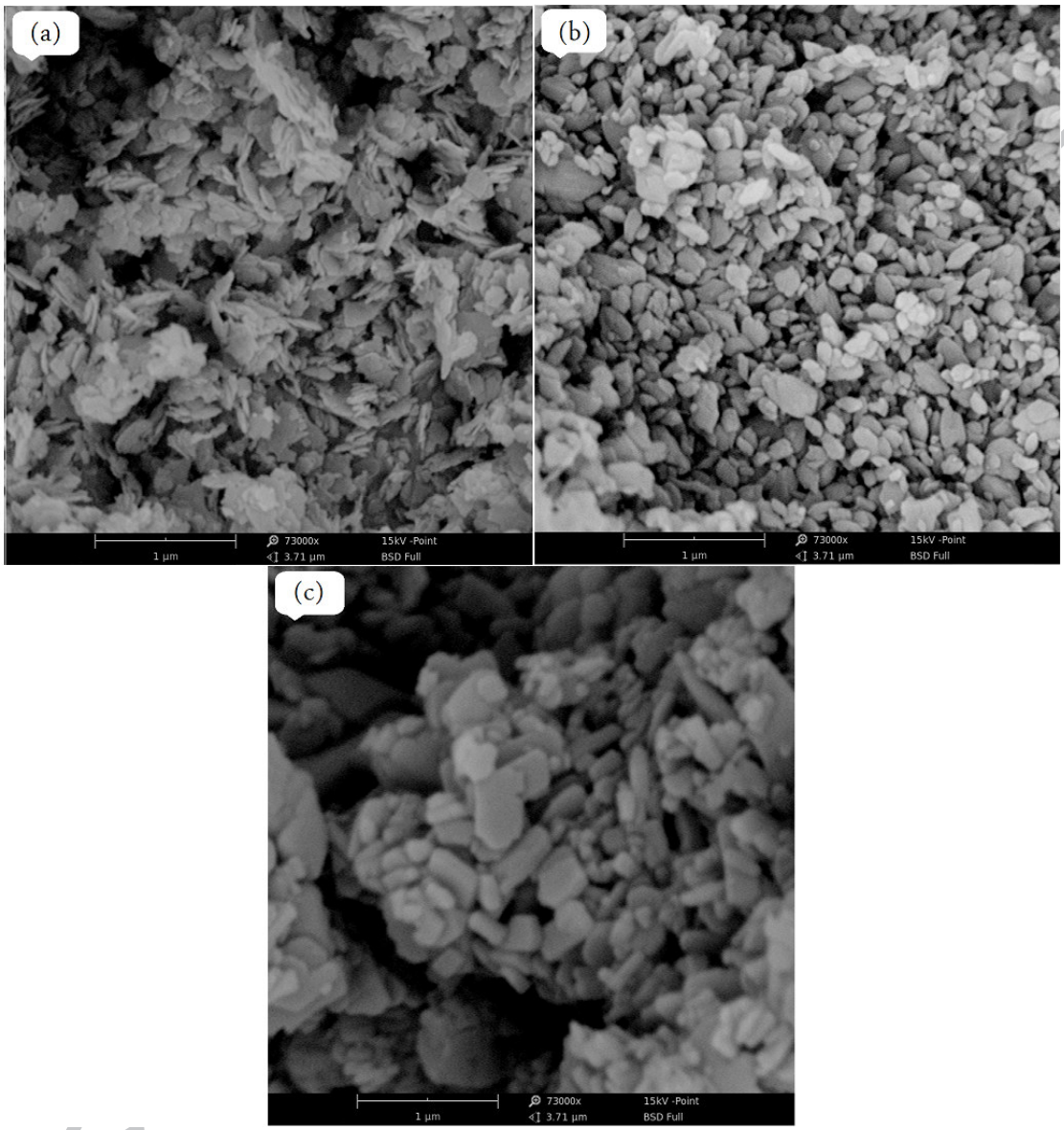

Fig. 8. FE-SEM images of DUT-32 micro/nano-structures prepared by sonochemical process where reagents concentrations are constant using a 40-W irradiation frequency in a 60-min time of sonication in the presence of two dissimilar modulators (3 ml): a) pyridine, b) acetic acid, and c) acetic acid + pyridine.

When the experimental results of the sonochemical process and the simulation results are compared using their powder X-ray diffraction (PXRD) patterns, it is corroborated that the sonochemically synthesized DUT-32 yields the same structure as the DUT-32 sample synthesized by conventional heating – as shown in Fig. 9.

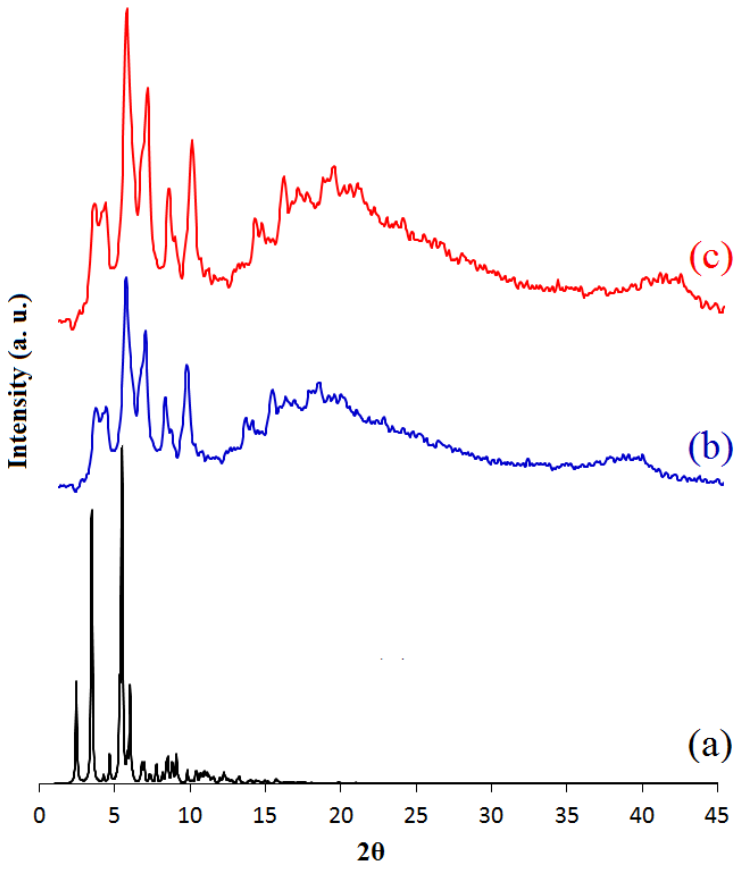

Fig. 9. PXRD patterns of DUT-32 micro/nano-structures, prepared by either conventional heating or sonochemical reaction: a) simulated DUT-32, b) DUT-32 conventional heating, and c) DUT-32-K nanoplates.

Fig. 10 compares the DUT-32-K nanostructures synthesized through the sonochemical process with the bulk material prepared by the solvothermal approach, and H_3BTCTB and 4,4´-BPDC

ligands in terms of their IR spectra. For the 4,4´-BPDC and H_3BTCTB ligands in the DUT-32 sample, characteristic adsorption bands are observed: Corresponding to DMF carbonyl group as the molecular guest some absorption bands with variable intensities are seen between 1340-1630 cm^{-1}. Corresponding to uncoordinated carboxylate of fumarate, absorption bands are observed at 1735 cm^{-1} [71]. FT-IR analyses have also been performed for samples of DUT-32 single crystals and DUT-32-K nanostructures. In all these two samples there are sharp peaks of 4,4´-BPDC and H_3BTCTB ligands between 1200 to 1600 cm^{-1}, which demonstrates that the two ligands are present in the DUT-32 structure.

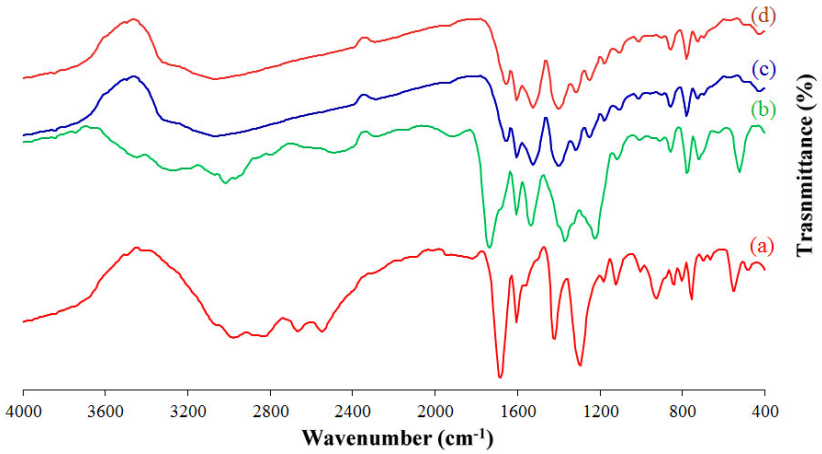

Fig. 10. Comparison of FTIR spectra of 4,4´-BPDC ligand (a), H_3BTCTB ligand (b), DUT-32 crystals (c), and DUT-32-K nanostructures (d) which is synthesized by solvothermal method, and morphology modified.

Fig. 11 the diagram of N_2 adsorption-desorption isotherm for DUT-32-K micro/nano-structures is shown. The trend is in agreement with that of mesoporous materials in the literature. Table 2 makes a comparison between this diagram and the BET surface area for the other samples in this study. According to the table, DUT-32-K exhibits the highest BET surface area and Drug loading

efficiency. In DUT-32-B micro/nano-structures, the amounts of the adsorbed N_2 and BET surface area are lower than those in sample of DUT-32-L and DUT-32 crystals. Apparently, when the modulator reagent is present during synthesis, the BET surface area of the DUT-32 compound is no longer negatively affected by the reduction in the size of the particles. Indeed, the totally flat branches of absorption are observed up to p/p = 0.9 as the porosity occurrence is disregarded. In this context, mesoporous materials are thus synthesized. As a result of the cage-shaped pores created from defects, a hysteric loop is likely to develop. According to literature, the synthesis route impact on the MOF porosity can be ascribed to the formation of structural defects [72, 73]. It follows then, that DUT-32-K must have larger/more defects than DUT-32-B and DUT-32-L, as a result of the modulator present during its synthesis. Consequently, based on the N_2 adsorption isotherm for the best sonochemically synthesized morphology (i.e. DUT-32-K), a slight improvement is observed for the BET surface area (4876 m^2/g) in comparison with prepared sample via hydrothermal and DUT-32-B and DUT-32-L micro/nano-structures synthesized via ultrasonic irradiation. Even so, a considerable challenge still exists as to explain how the shape, porosity, and especially the dispersion of the small mesoporous particles can be fully controlled [74-76].

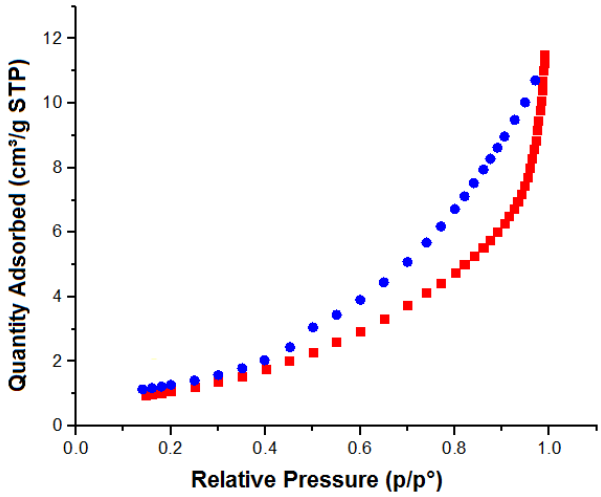

Fig. 11. N_2 adsorption-desorption isotherm collected at 77 K for DUT-32-K micro/nano-structures synthesized via ultrasonic irradiation in the presence of pyridine as a modulator.

Table 2

Drug loading content and drug loading efficiency of the DUT-32 samples.

Samples	Surface area	Drug loading content	Drug loading efficiency
DUT-32 crystals	4376	11.76	17.54
DUT-32-B	4107	9.73	15.32
DUT-32-K	4876	18.45	25.18
DUT-32-L	4522	14.08	20.95

Figs. 12 and 13 investigate the AMX removal efficiency of the same four DUT-32 samples placed in aqueous 20 ppm AMX solution for 120 min. 92% removal efficiency was observed after 120 min in the presence of the single crystals of DUT-32. This means that by use of the sonochemical synthesis methods nanoplates can be produced which remove more AMX from solution and faster than the single crystals, produced by the traditional hydrothermal synthesis method.

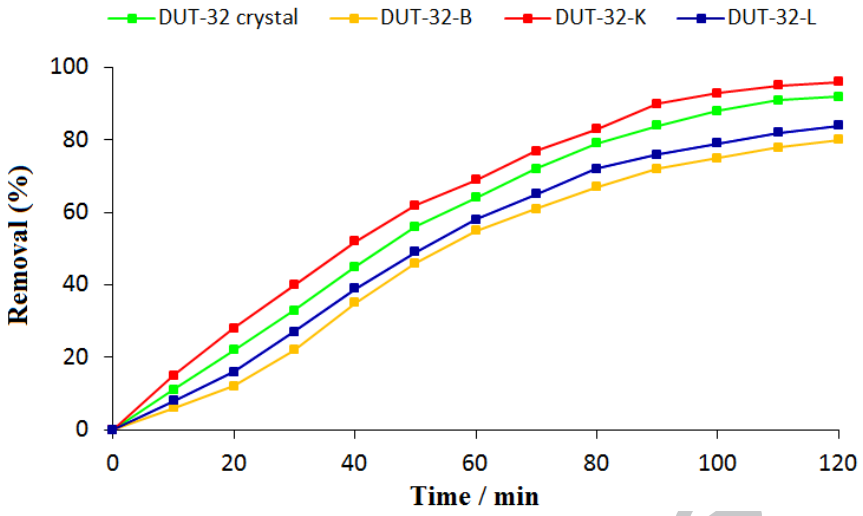

Fig. 12. Removal efficiency of AMX by four different DUT-32 samples, assessed using UV–Vis absorption spectroscopy.

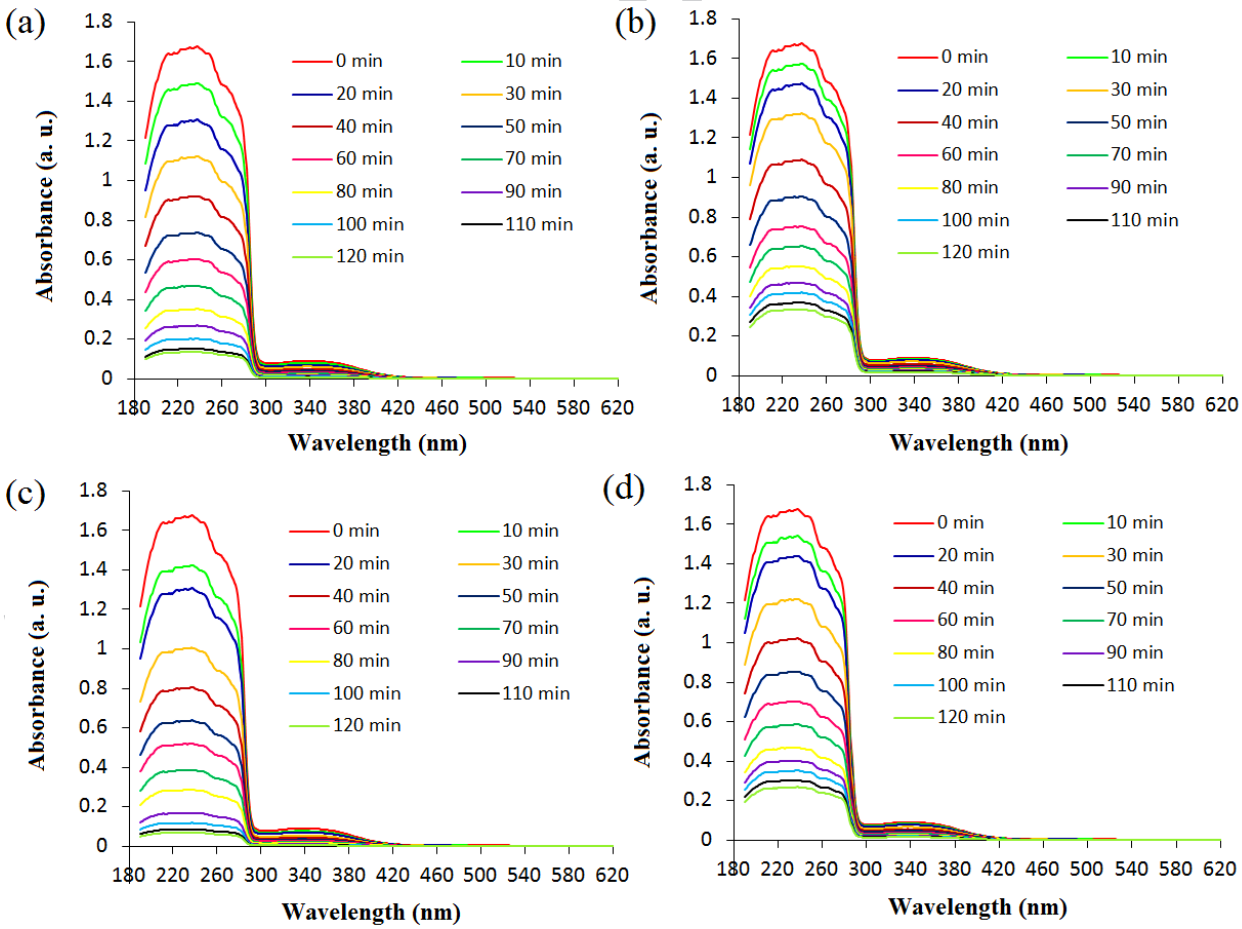

Fig. 13. UV–Vis absorption spectra of a solution of 20 ppm AMX in presence of (a) DUT-32 crystals, b) DUT-32-B, c) DUT-32-K, and d) DUT-32-L.

In the present study, the AMX removal kinetics in the suspended solutions, with DUT-32-K as the superior absorbent, has been investigated utilizing the kinetics of zero, first, and second order rate reactions – as shown in Fig. 14 and Table 3. Using this kinetics relation, as shown in Table 3, different correlation coefficients have been estimated. In this relation, the correlation coefficients of zero, first and second order rate equations are represented by R_0, R_1, and R_2, respectively. R_1 shows superior correlation with $K_1 = 0.0281$ min^{-1} with regard to the DUT-32-K nanostructures. In this context, it can be posited that first order reaction kinetics is conditioned by the removal of AMX from the MOF.

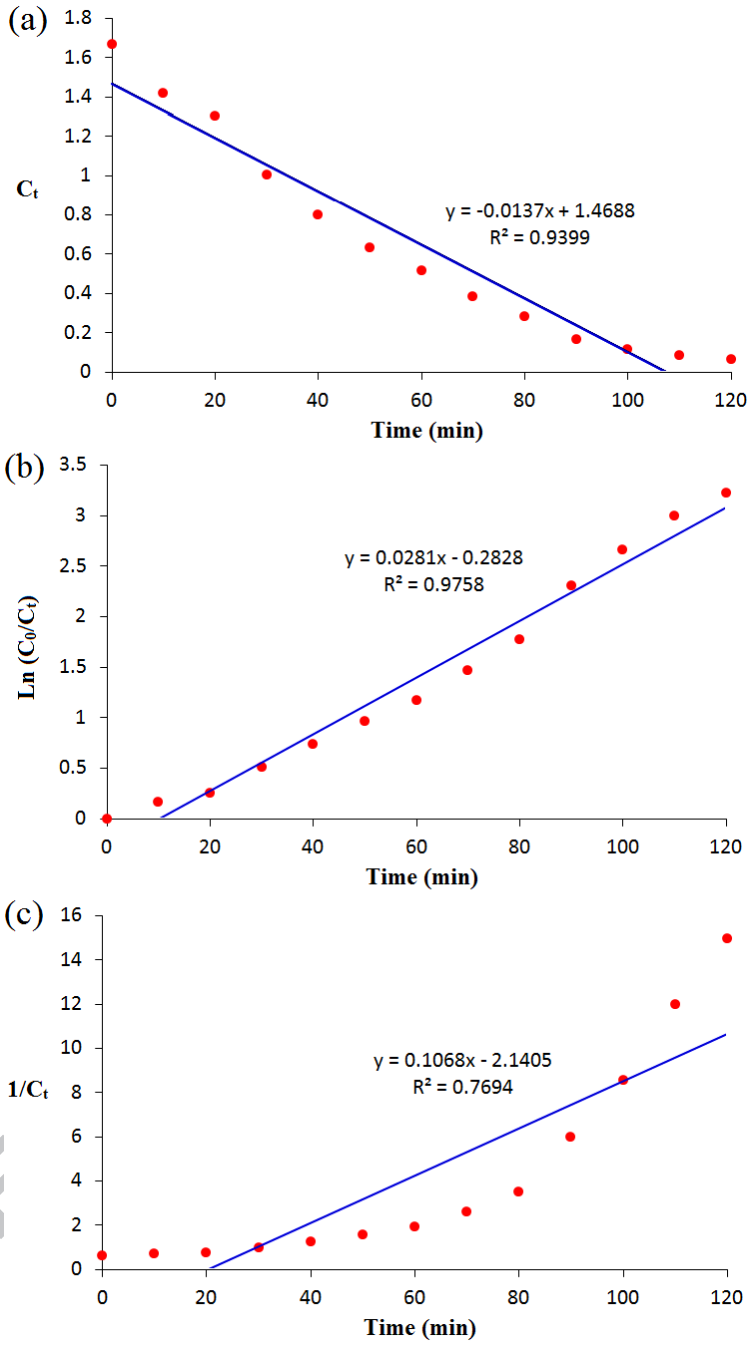

Fig. 14. Reaction kinetics of AMX removal for DUT-32-K micro/nano-structures, (a) zero (b) first and (c) second order.

Table 3

Kinetics parameters for different kinetic models for AMX removal using four different samples.

Samples	R_0	R_1	R_2	Order(s)	K_1 (min^{-1})
DUT-32 crystal	0.9454	0.9825	0.7839	y = 0.0268x - 0.2759	0.0268
DUT-32-B	0.9217	0.9677	0.7757	y = 0.0203x - 0.2463	0.0203
DUT-32-K	0.9399	0.9758	0.7694	y = 0.0281x - 0.2828	0.0281
DUT-32-L	0.9240	0.9583	0.7041	y = 0.0231x - 0.2609	0.0231

3.5. Doxorubicin hydrochloride loading and release

DOX, a typical anti-cancer drug, was introduced into DUT-32 to evaluate the loading and sustained release behaviors. According to the results (Table 2), the maximum DOX drug loading is achieved by DUT-32-K, which could be explained again by the increase in the DUT-32-K BET surface area, brought about by the structural defects introduced by the modulator. This surface area to drug loading capacity relationship is shown again by DUT-32-B possessing the smallest surface area and loading capacity. As reported in the literature, drug loading and drug release are both influenced by the various forces such as Van der Waals, coordination bonds, hydrogen bonds, electrostatic interactions and π-π interactions. Of these, electrostatic interactions are reported to have the most significant effect [77].

For ensuring that the system output in the physiological environment is in fact the drug, the release profile is analysed. The DOX release behavior at pH 7.4 and physiological temperature vs time for the four DUT-32 samples is shown in Fig. 15. The percentage of released guest molecules is calculated from data obtained using UV–Vis spectrophotometry (Fig. 16). As the time passes, a gradual growth in DOX concentration occurs, showing that DOX molecules are continuously released. Once again, the optimized DUT-32-K performed the best, releasing 54% of the DOX in 100 hours. A two-phase drug release behavior was observed, with a low initial burst release (within 24% of the loaded value) in 30 hours. The breaking of weaker drug-MOF

interactions on the DUT-32 exterior surface are responsible for the preliminary rapid release rate in 0-30 h. The guest drug molecules held in the interior pores are responsible for the sustained release of DOX with a decreased rate of release from 30 h to 100 h.

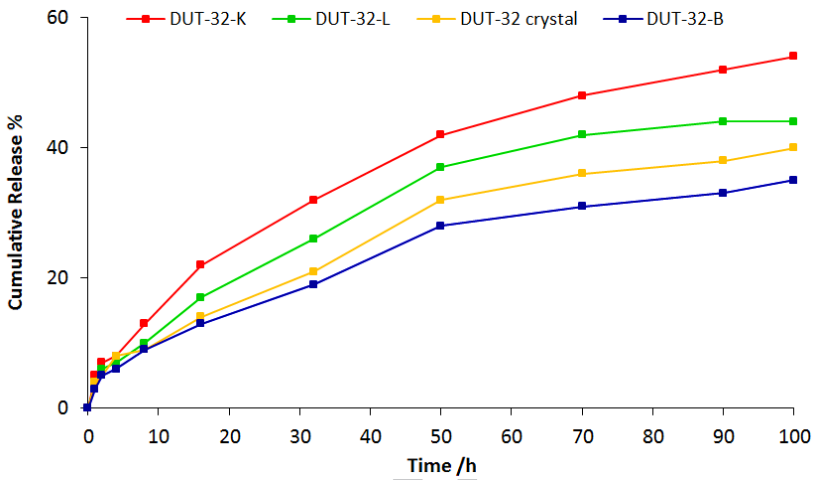

Fig. 15. The cumulative drug release of DOX from the four DUT-32 samples at pH of 7.4 and physiological temperature.

Fig. 16 shows a sorption band at 482 nm, which increases in intensity with lengthening of the release time due to DOX molecules cumulative release over time, demonstrating that nano/micro-DUT-32 is able to maintain the integrity of its crystalline structure at these conditions.

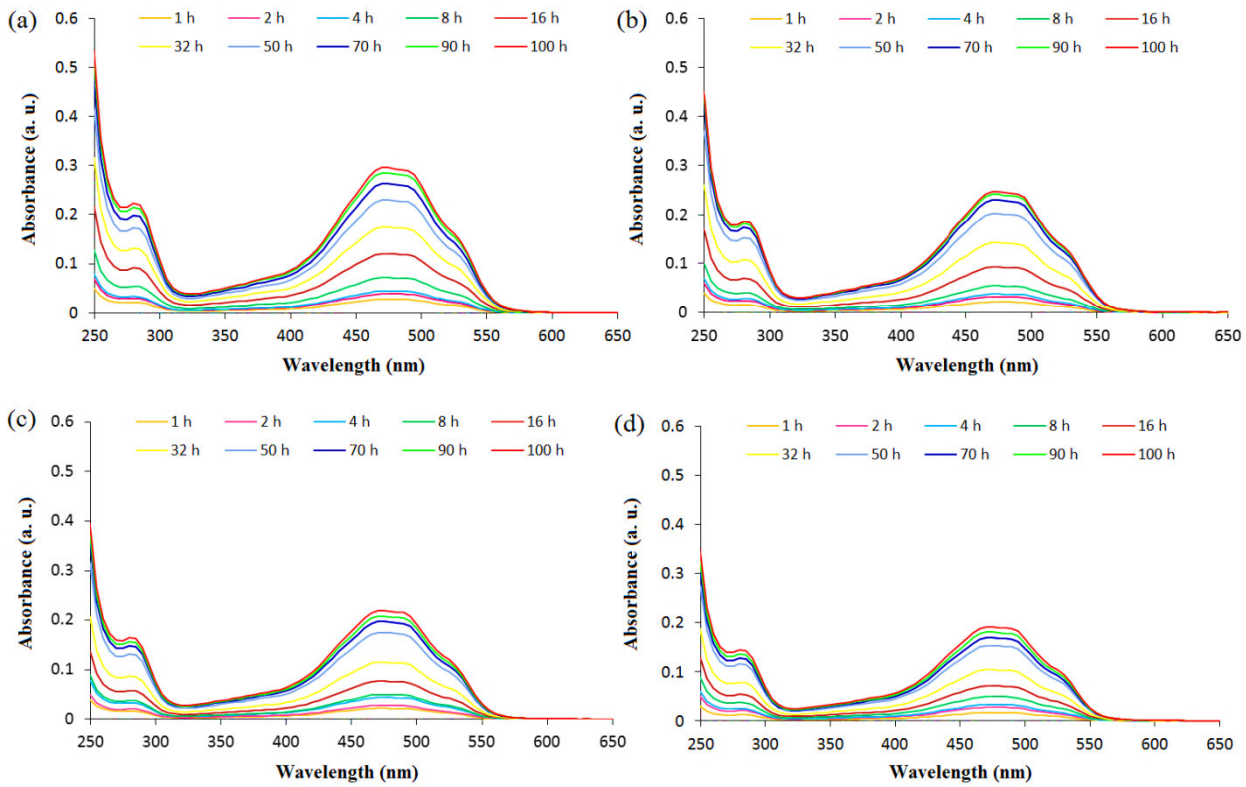

Fig. 16. UV/Vis absorption spectra of the DOX release through carriers of DUT-32-K (a), DUT-32-L (b), DUT-32 crystal (c), and DUT-32-B (d) at pH of 7.4 and physiological temperature.

A kinetic model of drug release can be provided (Fig. 17), as DUT-32 maintains the integrity of its framework in these test conditions. Progressive desorption from the pores is responsible for DOX release, so in accordance with the Fick diffusion law, the fitted data can be expressed through the single exponential function below (Eq. 5):

$$\mathrm{Ln}\,(1-M_t/M_\infty) = -kt \qquad \text{(Eq. 5)}$$

Here, release value at time t is shown by M_t, M_∞ signifies the maximum release, and k represents the first order release constant. Results of the fitted data demonstrate that the release constant K = 0.227 h^{-1} while R^2 = 0.9925.

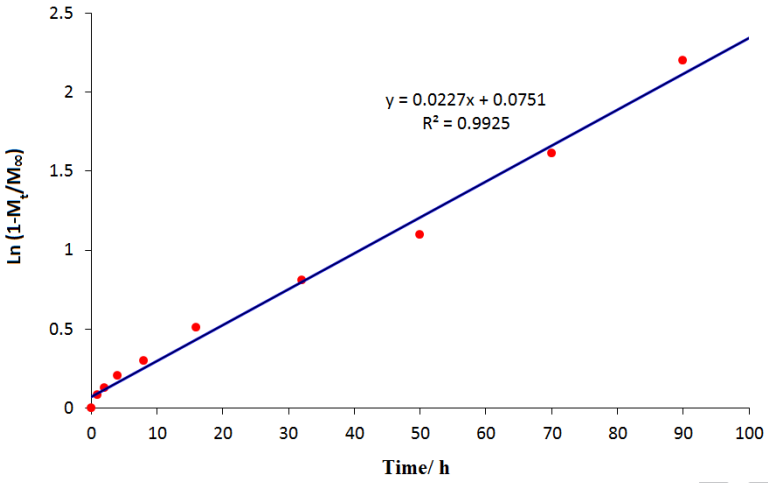

Fig. 17. Kinetic model of drug release of DOX from DOX/DUT-32-K plotted against time, in SBF solution and physiological temperature.

Decreasing the pH increases the rate of DOX released from DUT-32-K, indicating its dependency on pH. In this range of pH, drug release and change from physiological pH to lower, acidic pHs are described. Cancerous cells are slightly acidic with pH values of 4-6. Therefore, in a desired system of drug delivery, drug molecules ought to be released in this range of pH. MOFs are commonly stable at neutral pH, but in the acidic range, dissociation of the framework occurs as a result of ligand-metal ionic coordination becoming separated. Resultantly, at this acidic pH, an opportunity arises for the drug release. Fig. 18 a-c shows a constant growth in the intensity of UV–Vis spectra at 482 nm by the passing of time, thus indicating the molecular drug release from the framework of DUT-32. Because of DUT-32-K stability at pH 7.4, the drug release is very low and the intensity of UV–Vis spectra does not show any significant increase. This is an important observation as healthy cells pH is approximately 7.4, the MOF framework remains intact and a reduced drug release is observed. With the passage of 4 days, by pH variations from 7.4, 6, and 4.5 at 37 ℃, the final release rate of DOX might increase up to 54%,

83%, and 98%, respectively, which is perhaps due to ligands protonation by decreased pH. This in turn causes the electrostatic interaction between DUT-32-K functional groups and DOX to be dissociated. Resultantly, the incorporated DOX Is no longer held in place by a well structurally ordered MOF and is released from the samples. Both drug loading and drug release mechanisms and rates are affected by the carriers in drug delivery systems. Hence, great importance is attached to the provision of effective and inexpensive carriers in drug delivery systems, especially for practical pharmaceutical applications.

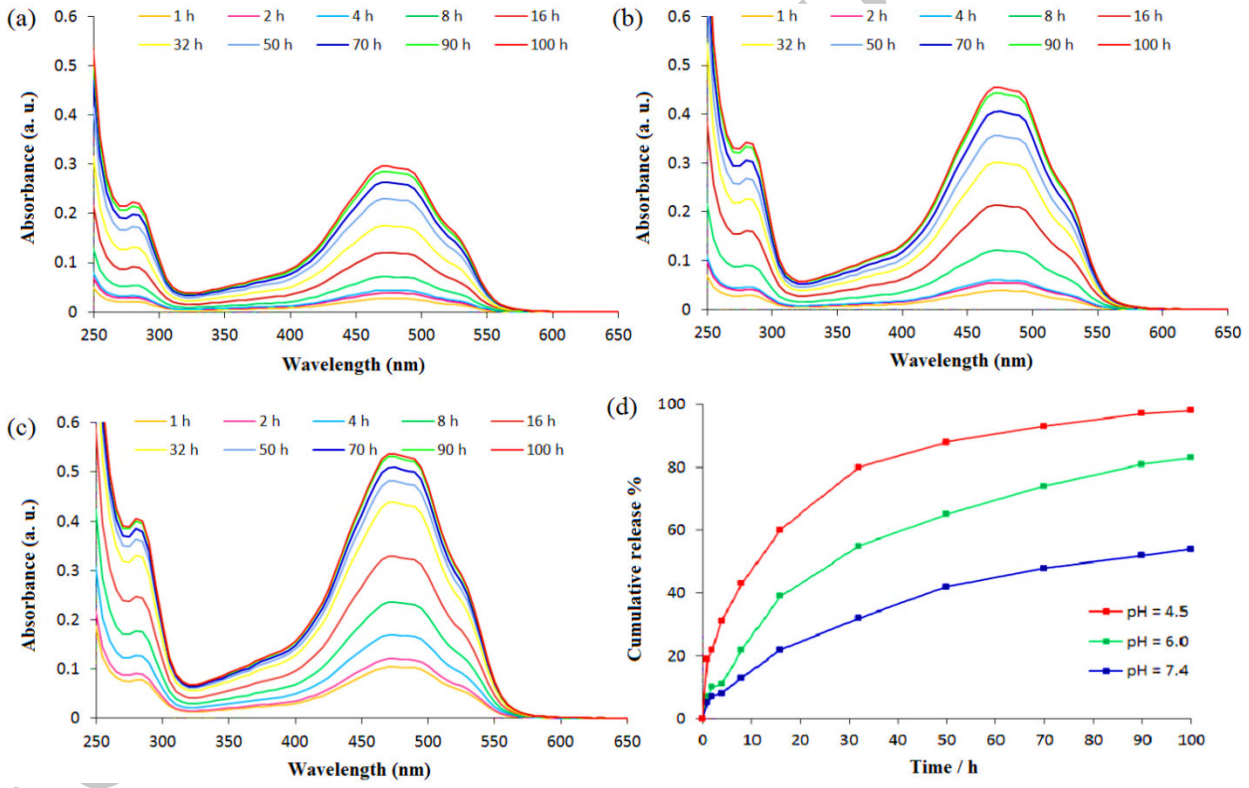

Fig. 18. Representative UV–Vis spectra of the release buffer of DUT-32-K micro/nano-structures with increasing time at pH = 7.4 (a), pH = 6 (b), and pH = 4.5 (c); cumulative DOX release (%) from DOX/DUT-32-K carrier at three different pHs (d).

FTIR spectra of the free DOX and the synthesized products are given in Fig. 19. A broad band around 3450 cm^{-1} can be observed, which is caused by the O–H stretching from the molecules of water [78, 79]. The band's broadness is in accord with the extensive hydrogen bonding of the non-coordinated and coordinated molecules of water [80]. The asymmetric and symmetric (OCO^-) stretching from the carboxylate groups are responsible for the observed bands at 1647 cm^{-1} and 1387 cm^{-1}. Because of the C=C stretching from the aromatic rings, a further band at 1597 is observed. The successful loading of DOX onto the surface of DUT-32-K was also proved by FTIR spectra (Fig. 19c) and the IR bands of DOX/DUT-32-K revealed characteristic modes of the DOX molecules: Firstly, the absorption bands of the C=C skeleton vibration at 1615 cm^{-1} and C–H out-of-plane bending vibration at 796 cm^{-1} correspond to the aromatic rings of DOX. The band observed at 1735 cm^{-1} is assigned to the C=O stretching of aldehydes group whereas the band at 1709 cm^{-1} corresponds to the C=O stretching of unsaturated esters. The band at 1064 cm^{-1} and 1104 cm^{-1} corresponds to the C–N stretching of aliphatic amines. Also, the N–H stretching band at 3320 cm^{-1} of free DOX, shifted to 3343 cm^{-1} in case of DOX/DUT-32-K. In addition, the adsorption of DOX onto DUT-32-K surfaces was distinctive, as evidenced by a larger peak at 1594 cm^{-1}, assigned to the C=O bond at the 13-keto position of DOX [81].

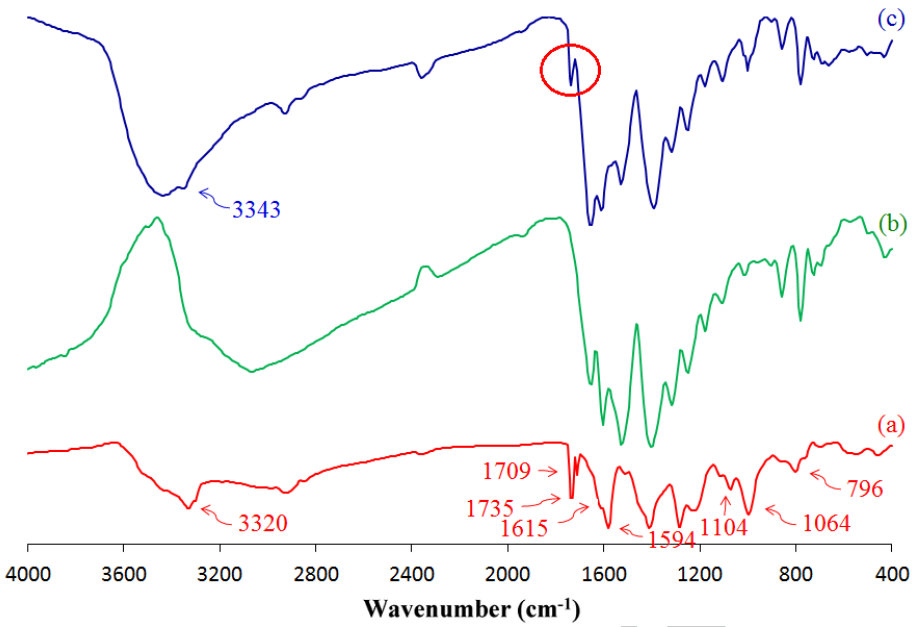

Fig. 19. Comparison of IR spectra of free DOX (a), DUT-32-K nanostructures (b), and DOX/DUT-32-K (c).

The adsorption process results from the interaction between the guest molecule and the adsorbent material, in our case, the DUT-32 and DOX. Generally, these MOF-drug interactions are weak physisorption interactions. However, in some cases, the interactions between the host and the guest molecules are strong, and resultantly structural changes and chemisorption and are likely to happen. Accordingly, a viable tool for the study of such crystalline transformations will be the PXRD. The experimental powder pattern of DUT-32-K in DOX is shown by the red line in Fig. 20. Expectedly, all of the peaks which are associated with the $[Zn_4O(BPDC)(BTCTB)_{4/3}(DEF)_{39.7}(H_2O)_{11.3}]$ structure prepared by Kaske et al. are shown in this diffractogram [68]. In Fig. 20, PXRD data for the DUT-32-K sample are shown in green color. In spite of the still retaining strong crystallinity, a structural variation in DUT-32 can be observed during the incorporation process, which is likely to be caused by the supra-molecular interactions of the MOF and the drug. The intense signals at 2θ values of 25.96, 14.08, and 9.82

which are related to the miller indices [220], [002], and [102] respectively in DOX, which confirms the drugs incorporation into the DUT-32 structure. This finding is in agreement with the results in the literature [82] and with the IR-spectroscopy results. When the test of dissolution is completed, the release of the incorporated DOX occurs. Afterwards, as shown in Fig. 20c in blue, the powder pattern is collected. As we have expected, no diffraction peaks corresponding to the drug were observed. This observation fits with the results of the dissolution test. Similarly, the structural variations of the DUT-32-K have here been detected, where a slight amorphization has been seen in the structure.

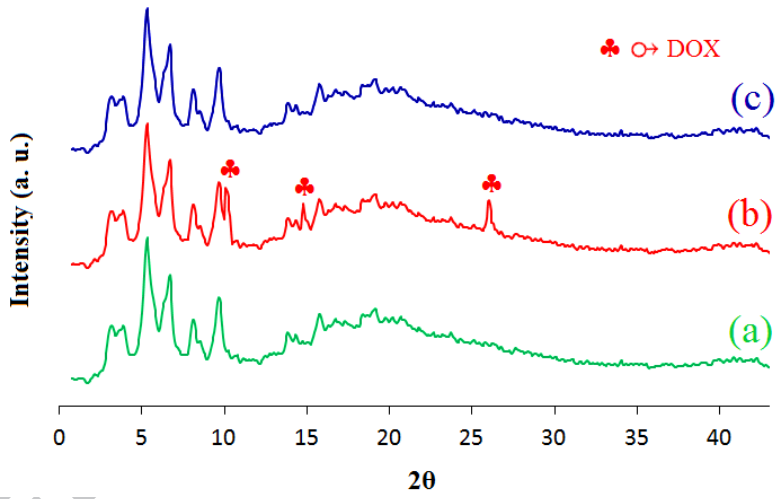

Fig. 20. XRD patterns of DUT-32-K micro/nano-structures before release test (green line) DOX/DUT-32-K (red line), and DUT-32-K micro/nano-structures after release test (blue line).

3.6.In vitro cytotoxicity

After the drug molecules of DOX are encapsulated into DUT-32-K frameworks, both DUT-32-K and drug-loaded DUT-32-K (i.e. DOX/DUT-32-K) were explored in terms of their biocompatibility. Using MTT assays, the cytotoxic effects of DOX/DUT-32-K and free DOX

were compared. According to Fig. 21, as the concentrations of DOX/DUT-32-K and free DOX increase from 0.3125 to 40 μg ml^{-1}, so do their cytotoxic effects on prostate cancer cell line (PC3) and cervical cancer cell line (HeLa). Under a shared 24-hour culture, the DOX/DUT-32-K is observed to cause PC3 and HeLa cells death analogous to the free DOX. With their shared culture for 72 h, in all concentrations with the exception of 0.3125 μg ml^{-1}, DOX/DUT-32-K demonstrates more cytotoxic effects than free DOX. This increase in DOX/DUT-32-K cytotoxicity, compared to free DOX, is primarily caused by the constant release of the molecular drug from the MOF frameworks as well as the enhanced DOX uptake by the loaded cells in DUT-32-K frameworks. Furthermore, the intact DUT-32-K micro/nano-structures biocompatibility has been investigated. Different DUT-32-K concentrations have been incubated for 24 h and 72 h with PC3 and HeLa cells, and assessment of the cells viability has then been performed. In the tested range of concentrations and even as it rises to 40 μg ml^{-1}, biocompatible DUT-32-K micro/nano-structures does not show any drastic effects upon the viability of the cells, and thus it can be posited that DUT-32-K has no cytotoxic impact – as shown in Fig. 21.

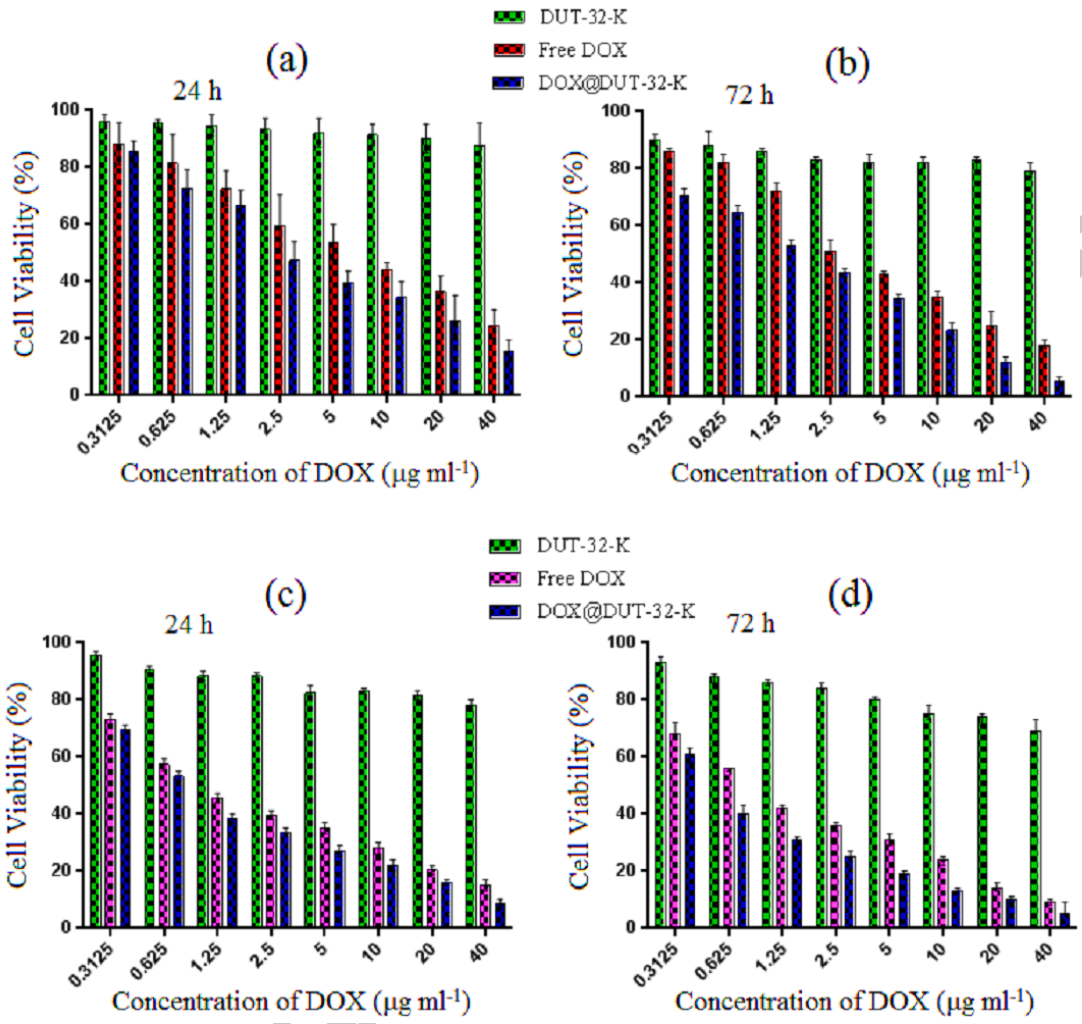

Fig. 21. Comparison of the cytotoxic effects of DUT-32-K, DOX/DUT-32-K, and free DOX on cells viability evaluated by incubating various concentrations of samples for 24 h and 72 h with HeLa cells (a and b) and PC-3 cells (c and d).

4. Conclusion

In this study, regular nanoplates of the MOF DUT-32 were prepared through the use of sonication and a pyridine modulator. During the optimization process, it was found that sonication time, reagent concentration, irradiation frequency and modulator composition/concentration all effected the shape, size and morphology of the nanostructures

formed. It was also found that the nanostructures formed with the most regular size and morphology also possessed the highest BET surface area, likely as a result of the modulator creating additional/larger internal defects. This more regular particle size and/or larger surface area also lead the optimized sample (DUT-32-K) to have the highest AMX absorption and most favorable DOX release behavior. Not only was the MOF shown to hold its structure at physiological conditions, but it was shown to increase its release efficiency from 54% to 98% (after 100 hours) in pHs 7.4 to 4.5 respectively. Furthermore, the DOX loaded DUT-32-K was shown to kill cancerous cells just as efficiently as free DOX and the DUT-32-K alone was shown in a viability study to have a low cytotoxicity to healthy cells. These results show that not only are these DUT-32-K nanostructures capable of efficient drug loading and of a tumor specific release, but are also able to mop up environmentally harmful POPs (AMX) from water sources, where they are ubiquitous.

Acknowledgement

Support of this investigation by Tarbiat Modares University is gratefully acknowledged.

References

[1] F. Fouladi, K. J. Steffen, S. Mallik, Enzyme-Responsive Liposomes for the Delivery of Anticancer Drugs. Bioconjugate Chem. 28 (2017) 857–868.

[2] L. Carlino, G. Rastelli, Dual Kinase-Bromodomain Inhibitors in Anticancer Drug Discovery: A Structural and Pharmacological Perspective. J. Med. Chem. 59 (2016) 9305−9320.

[3] S. F. Fonseca, N. B. Padilha, S. Thurow, J. A. Roehrs, L. Savegnago, M. N. de Souza, M. G. Fronza, T. Collares, J. Buss, F. K. Seixas, D. Alves, E. J. Lenardão, Ultrasound-promoted

copper-catalyzed synthesis of bis-arylselanyl chrysin derivatives with boosted antioxidant and anticancer activities, Ultrason. Sonochem. 39 (2017) 827–836.

[4] H. R. Kim, D. G. You, S.-J. Park, K.-S. Choi, W. Um, J.-H. Kim, J. H. Park, Y.-S. Kim, MRI monitoring of tumor-selective anticancer drug delivery with stable thermosensitive liposomes triggered by high-intensity focused ultrasound. Mol. Pharmaceutics 13 (2016) 1528–1539.

[5] U. N. Pan, R. Khandelia, P. Sanpui, S. Das, A. Paul, A. Chattopadhyay, Protein-Based Multifunctional Nanocarriers for Imaging, Photothermal Therapy, and Anticancer Drug Delivery. ACS Appl. Mater. Interfaces 9 (2017) 19495–19501.

[6] X. Yang, H. Du, J. Liu, G. Zhai, Advanced nanocarriers based on heparin and its derivatives for cancer management. Biomacromolecules 16 (2015) 423–436..

[7] X. Cui, X. Guan, S. Zhong, J. Chen, H. Zhu, Z. Li, F. Xu, P. Chen, H. Wang, Multi-stimuli responsive smart chitosan-based microcapsules for targeted drug delivery and triggered drug release, Ultrason. Sonochem. 38 (2017) 145–153.

[8] L. Qiu, M. Zhu, K. Gong, H. Peng, L. Ge, L. Zhao, J. Chen, pH-triggered degradable polymeric micelles for targeted anti-tumor drug delivery, Mater. Sci. Eng., C 78 (2017) 912–922.

[9] W. Cai, C.-C. Chu, G. Liu, Y.-X. J. Wang, Metal–Organic Framework-Based Nanomedicine Platforms for Drug Delivery and Molecular Imaging. Small 11 (2015) 4806–4822.

[10] G.-J. Ding, Y.-J. Zhu, C. Qi, B.-Q. Lu, F. Chen, J. Wu, Porous hollow microspheres of amorphous calcium phosphate: soybean lecithin templated microwaveassisted hydrothermal synthesis and application in drug delivery, *J. Mater. Chem. B,* 3 (2015) 1823–1830.

[11] L. Zhu, M. Li, X. Liu, Y. Jin, Drug-Loaded PLGA Electrospraying Porous Microspheres for the Local Therapy of Primary Lung Cancer via Pulmonary Delivery. ACS Omega 2 (2017) 2273–2279.

[12] X. Zheng, L. Wang, Q. Pei, S. He, S. Liu, Z. Xie, Metal–Organic Framework/Porous Organic Polymer Nanocomposite for Photodynamic Therapy, Chem. Mater. 29 (2017) 2374–2381.

[13] A. R. Abbasi, M. Rizvandi, Influence of the ultrasound-assisted synthesis of Cu–BTC metal–organic frameworks nanoparticles on uptake and release properties of rifampicin, Ultrason. Sonochem. 40 (2018) 465–471.

[14] R. Yasmin, S. Rao, K. Bremmell, C. Prestidge, Synergistic role of solid lipid and porous silica in improving the oral delivery of weakly basic poorly water soluble drugs, Eur. J. Pharm. Sci. 96 (2017) 508–514.

[15] W. Zhang, Y. Liu, G. Lu, Y. Wang, S. Li, C. Cui, J. Wu, Z. Xu, D. Tian, W. Huang, J. S. DuCheneu, W. D. Wei, H. Chen, Y. Yang, F. Huo, Mesoporous Metal–Organic Frameworks with Size-, Shape-, and Space-Distribution-Controlled Pore Structure. Adv. Mater. 27 (2015) 2923–2929.

[16] H. Wang, H. Y. Jeong, M. Imura, L. Wang, L. Radhakrishnan, N. Fujita, T. Castle, O. Terasaki, Y. Yamauchi, Shape- and Size-Controlled Synthesis in Hard Templates: Sophisticated Chemical Reduction for Mesoporous Monocrystalline Platinum Nanoparticles. *J. Am. Chem. Soc*. 133 (2011) 14526–14529.

[17] S. M. Mousavi, A. R. Mahjoub, R. Abazari, Facile green fabrication of nanostructural Ni-doped ZnO hollow sphere as an advanced photocatalytic material for dye degradation, J. Mol. Liq. 242 (2017) 512–519.

[18] F. Xue, Y. Wen, P. Wei, Y. Gao, Z. Zhou, S. Xiaoc, T. Yi, A smart drug: a pH-responsive photothermal ablation agent for Golgi apparatus activated cancer therapy. Chem. Commun. 53 (2017) 6424–6427.

[19] X. Sun, R. Du, L. Zhang, G. Zhang, X. Zheng, J. Qian, X. Tian, J. Zhou, J. He, Y. Wang, Y. Wu, K. Zhong, D. Cai, D. Zou, Z. Wu, A pH-Responsive Yolk-Like Nanoplatform for Tumor Targeted Dual-Mode Magnetic Resonance Imaging and Chemotherapy. ACS Nano 11 (2017) 7049–7059.

[20] E. Ellis, K. Zhang, Q. Lin, E. Ye, A. Poma, G. Battaglia, X. J. Loh, T.-C. Lee, Biocompatible pH-responsive nanoparticles with a core-anchored multilayer shell of triblock copolymers for enhanced cancer therapy. J. Mater. Chem. B 5 (2017) 4421–4425.

[21] S. Khoee, A. Saadatinia, R. Bafkary, Ultrasound-assisted synthesis of pH-responsive nanovector based on PEG/ chitosan coated magnetite nanoparticles for 5-FU delivery, Ultrason. Sonochem. 39 (2017) 144–152.

[22] G. E. Cinay, P. Erkoc, M. Alipour, Y. Hashimoto, Y. Sasaki, K. Akiyoshi, S. Kizilel, Nanogel-integrated pH Responsive Composite Hydrogels for Controlled Drug Delivery. ACS Biomater. Sci. Eng. 3 (2017) 370–380.

[23] B. Li, Z. Meng, Q. Li, X. Huang, Z. Kang, H. Dong, J. Chen, J. Sun, Y. Dong, J. Li, X. Jia, J. L. Sessler, Q. Meng, C. Li, A pH responsive complexation-based drug delivery system for oxaliplatin. Chem. Sci. 8 (2017) 4458–4464.

[24] X. Guan, Z. Guo, T. Wang, L. Lin, J. Chen, H. Tian, X. Chen, A pH-Responsive Detachable PEG Shielding Strategy for Gene Delivery System in Cancer Therapy. *Biomacromolecules 18 (*2017) 1342–1349.

[25] S. Maher, A. Santos, T. Kumeria, G. Kaur, M. Lambert, P. Forward, A. Evdokiou, D. Losic, Multifunctional microspherical magnetic and pH responsive carriers for combination anticancer therapy engineered by droplet-based microfluidics. J. Mater. Chem. B 5 (2017) 4097–4109.

[26] T. A. Ternes, M. Meisenheimer, D. McDowell, F. Sacher, H.-J. Brauch, B. H.-Gulde, G. Preuss, Uwe Wilme, N. Z.-Seibert, Removal of Pharmaceuticals during Drinking Water Treatment. Environ. Sci. Technol. 36 (2002) 3855–3863.

[27] S. Liu, H. Zhao, H.-J. Lehmler, X. Cai, J. Chen, Antibiotic Pollution in Marine Food Webs in Laizhou Bay, North China: Trophodynamics and Human Exposure Implication. Environ. Sci. Technol. 51 (2017) 2392–2400.

[28] E. A. Serna-Galvis, J. Silva-Agredo, A. L. Giraldo-Aguirre, O. A. Flórez-Acosta, R. A. Torres-Palma, High frequency ultrasound as a selective advanced oxidation process to remove penicillinic antibiotics and eliminate its antimicrobial activity from water, Ultrason. Sonochem. 31 (2016) 276–283.

[29] I. M. Herzog, M. Fridman, Design and synthesis of membrane-targeting antibiotics: from peptides- to aminosugar-based antimicrobial cationic amphiphiles. Med. Chem. Commun. 5 (2014) 1014–1026.

[30] A.F. Martins, F. Mayer, E.C. Confortin, C.D. Frank, A Study of Photocatalytic Processes Involving the Degradation of the Organic Load and Amoxicillin in Hospital Wastewater. Clean 2009, 37, 365–371.

[31] X. Meng, C. J. Earnshaw, A. Tailor, R. E. Jenkins, J. C. Waddington, P. Whitaker, N. S. French, D. J. Naisbitt, B. K. Park, Amoxicillin and Clavulanate Form Chemically and Immunologically Distinct Multiple Haptenic Structures in Patients. Chem. Res. Toxicol. 29 (2016) 1762−1772.

[32] R. Andreozzi, V. Caprio, C. Ciniglia, M. De Champdoré, R. Lo Giudice, R. Marotta, E. Zuccato, Environ. Sci. Technol. 38 (2004) 6832–6838.

[33] E. Nägele, R. Moritz, Structure Elucidation of Degradation Products of the Antibiotic Amoxicillin with Ion Trap MSn and Accurate Mass Determination by ESI TOF. J. Am. Soc. Mass. Spectrom. 16 (2005) 1670–1676.

[34] X. Jin, X. Wang, Y. Wang, H. Ren, Oxidative Degradation of Amoxicillin in Aqueous Solution with Contact Glow Discharge Electrolysis. Ind. Eng. Chem. Res. 52 (2013) 9726–9730.

[35] K. H. Y. Hsi, A. J. Concepcion, M. Kenny, A. A. Magzoub, A. S. Myerson, Purification of amoxicillin trihydrate by impuritycoformer complexation in solution. CrystEngComm 15 (2013) 6776–6781.

[36] F. A. Ibrahim, J. J. M. Nasr, Direct determination of ampicillin and amoxicillin residues in food samples after aqueous SDS extraction by micellar liquid chromatography with UV detection. Anal. Methods 6 (2014) 1523–1529.

[37] E.K. Putra, R. Pranowo, J. Sunarso, N. Indraswati, S. Ismadji, Performance of activated carbon and bentonite for adsorption of amoxicillin from wastewater: Mechanisms, isotherms and kinetics. *Water Res*. 43 (2009) 2419–2430.

[38] T. R. Cook, Y.-R. Zheng, P. J. Stang, Metal–Organic Frameworks and Self-Assembled Supramolecular Coordination Complexes: Comparing and Contrasting the Design, Synthesis, and Functionality of Metal–Organic Materials. Chem. Rev. 113 (2013) 734–777.

[39] K. Sorachoti, B. Pangkumhang, V. Tanboonchuy, S. Tulaphol, N. Grisdanurak, Reversible adsorption of metalworking fluids (MWFs) on Cu-BTC metal organic framework, Chin. J. Chem. Eng. 25 (2017) 768–774.

[40] T. Islamoglu, S. Goswami, Z. Li, A. J. Howarth, O. K. Farha, J. T. Hupp, Postsynthetic Tuning of Metal–Organic Frameworks for Targeted Applications. Acc. Chem. Res. 50 (2017) 805–813.

[41] Q.-G. Zhai, X. Bu, X. Zhao, D.-S. Li, P. Feng, Pore Space Partition in Metal–Organic Frameworks. *Acc. Chem. Res*. 50 (2017) 407–417.

[42] P. Horcajada, R. Gref, T. Baati, P. K. Allan, G. Maurin, P. Couvreur, G. FErey, R. E. Morris, C. Serre, Metal Organic Frameworks in Biomedicine, Chem. Rev. 112 (2012) 1232–1268.

[43] C. O.-Tavra, E. F. Baxter, T. Tian, T. D. Bennett, N. K. H. Slater, A. K. Cheethamb, D. Fairen-Jimenez, Amorphous metal–organic frameworks for drug delivery, Chem. Commun. 51 (2015) 13878–13881.

[44] B. Liu, Y. He, L. Han, V. Singh, X. Xu, T. Guo, F. Meng, X. Xu, P. York, Z. Liu, J. Zhang, Microwave-assisted rapid synthesis of #-cyclodextrin metalorganic frameworks for size control and efficient drug loading. Cryst. Growth Des. 17 (2017) 1654–1660.

[45] D. J. Levine, T. Runcevski, M. T. Kapelewski, B. K. Keitz, J. Oktawiec, D. A. Reed, J. A. Mason, H. Z. H. Jiang, K. A. Colwell, C. M. Legendre, S. A. FitzGerald, J. R. Lon, Olsalazine-Based Metal–Organic Frameworks as Biocompatible Platforms for H_2 Adsorption and Drug Delivery. J. Am. Chem. Soc. 138 (2016) 10143–10150.

[46] J. Della Rocca, D. Liu, W. Lin, Nanoscale Metal–Organic Frameworks for Biomedical Imaging and Drug Delivery. Acc. Chem. Res. 44 (2011) 957–968.

[47] R.C. Huxford, J. Della Rocca, W. Lin, Metal-organic frameworks as potential drug carriers. Curr. Opin. Chem. Biol. 14 (2010) 262–268.

[48] C. He, K. Lu, D. Liu, W. Lin, Nanoscale Metal–Organic Frameworks for the Co-Delivery of Cisplatin and Pooled siRNAs to Enhance Therapeutic Efficacy in Drug-Resistant Ovarian Cancer Cells. J. Am. Chem. Soc. 136 (2014) 5181–5184.

[49] P. Horcajada, C. Serre, G. Maurin, N.A. Ramsahye, F. Balas, M. Vallet-Regí, M. Sebban, F. Taulelle, G. Ferey, Flexible Porous Metal-Organic Frameworks for a Controlled Drug Delivery. J. Am. Chem. Soc. 130 (2008) 6774–6780.

[50] P. Horcajada, C. Serre, M. Vallet-Regí, M. Sebban, F. Taulelle, G. F_erey, Metal-organic frameworks as efficient materials for drug delivery. Angew. Chem. Int. Ed. 45 (2006) 5974–5978.

[51] C. Gao, H. Zheng, L. Xing, M. Shu, S. Che, Designable Coordination Bonding in Mesopores as a pH-Responsive Release System. Chem. Mater. 22 (2010) 5437–5444.

[52] H. Bunzen, M. Grzywa, M. Hambach, S. Spirkl, D. Volkmer, From Micro to Nano: A Toolbox for Tuning Crystal Size and Morphology of Benzotriazolate-Based Metal–Organic Frameworks. Cryst. Growth Des. 16 (2016) 3190–3197.

[53] W. Xia, A. Mahmood, R. Zou, Q. Xu, Metal–organic frameworks and their derived nanostructures for electrochemical energy storage and conversion. Energy Environ. Sci. 8 (2015) 1837–1866.

[54] L. Wang, Y. Guan, X. Qiu, H. Zhu, S. Pan, M. Yu, Q. Zhang, Efficient ferrite/Co/porous carbon microwave absorbing material based on ferrite@metal–organic framework, Chem. Eng. J. 326 (2017) 945–955.

[55] P. Li, S.-Y. Moon, M. A. Guelta, L. Lin, D. A. Gomez-Gualdron, R. Q. Snurr, S. P. Harvey, J. T. Hupp, O. K. Farha, Nanosizing a Metal–Organic Framework Enzyme Carrier for Accelerating Nerve Agent Hydrolysis. ACS Nano 10 (2016) 9174–9182.

[56] Y. Chen, X. Huang, S. Zhang, S. Li, S. Cao, X. Pei, J. Zhou, X. Feng, B. Wang, Shaping of metal-organic frameworks: from fluid to shaped bodies and robust foams. J. Am. Chem. Soc. 138 (2016) 10810–10813.

[57] M. Krüger, A. K. Inge, H. Reinsch, Y.-H. Li, M. Wahiduzzaman, C.-H. Lin, S.-L. Wang, G. Maurin, O. Stock, Polymorphous Al-MOFs Based on V-Shaped Linker Molecules: Synthesis, Properties, and in Situ Investigation of Their Crystallization. Inorg. Chem. 56 (2017) 5851–5862.

[58] W. Yan, L.-J. Han, H.-L. Jia, K. Shen, T. Wang, H.-G. Zheng, Three Highly Stable Cobalt MOFs Based on "Y"-Shaped Carboxylic Acid: Synthesis and Absorption of Anionic Dyes. Inorg. Chem.55 (2016) 8816–8821.

[59] R. Feng, Y. Zhao, C. Zhu, T. J. Mason, Enhancement of ultrasonic cavitation yield by multi-frequency sonication, Ultrason. Sonochem. 9 (2002) 231–236.

[60] N. A. Khan, S. H. Jhung, Synthesis of metal-organic frameworks (MOFs) with microwave or ultrasound: rapid reaction, phase-selectivity, and size reduction, Coord. Chem. Rev. 285 (2015) 11–23.

[61] N. Stock, S. Biswas, Synthesis of Metal-Organic Frameworks (MOFs): Routes to Various MOF Topologies, Morphologies, and Composites. Chem. Rev. 112 (2012) 933–969.

[62] C. G. Carson, A. J. Brown, D. S. Sholl, S. Nair, Sonochemical Synthesis and Characterization of Submicrometer Crystals of the MetalOrganic Framework Cu[(hfipbb)(H_2hfipbb)$_{0.5}$]. Cryst. Growth Des. 11 (2011) 4505–4510.

[63] M. Díaz-García, A. Mayoral, I. Díaz, M. Sanchez-Sanchez, Nanoscaled M-MOF-74 Materials Prepared at Room Temperature. Cryst. Growth Des. 14 (2014) 2479−2487.

[64] N. Stock, S. Biswas, Synthesis of Metal-Organic Frameworks (MOFs): Routes to Various MOF Topologies, Morphologies, and Composites. Chem. Rev. 112 (2012) 933–969.

[65] Y. Chen, C. Yang, X. Wang, J. Yang, J. Li, Vapor phase solvents loaded in zeolite as the sustainable medium for the preparation of Cu-BTC and ZIF-8, Chem. Eng. J. 313 (2017) 179–186.

[66] M. Díaz-García, A. Mayoral, I. Díaz, M. Sanchez-Sanchez, Nanoscaled M-MOF-74 Materials Prepared at Room Temperature. Cryst. Growth Des. 14 (2014) 2479−2487.

[67] Y. Shiraishi, H. Tomita, K. Fujiki, H. Hirai, One-step synthesis of 4,4'-biphenyldicarboxylic acid from biphenyl using cyclodextrin as catalyst. React. Funct. Polym. 36 (1998) 99−102.

[68] R. Grunker, V. Bon, P. Muller, U. Stoeck, S. Krause, U. Mueller, I. Senkovska, S. Kaskel, A new metal–organic framework with ultra-high surface area. Chem. Commun. 50 (2014) 3450−3452.

[69] M. Gharib, V. Safarifard, A. Morsali, Ultrasound assisted synthesis of amide functionalized metal-organic framework for nitroaromatic sensing, 2017, in press.

[70] W.-J. Son, J. Kim, J. Kim, W.-S. Ahn, Sonochemical synthesis of MOF-5, Chem. Commun. 6336–6338 (2008).

[71] F. Zhou, J. Zhou, X. Gao, C. Kong, L. Chen, Facile synthesis of MOFs with uncoordinated carboxyl groups for selective CO_2 capture via postsynthetic covalent modification. RSC Adv. 7 (2017) 3713–3719.

[72] G. Barin, V. Krungleviciute, O. Gutov, J. T. Hupp, T. Yildirim, O. K. Farha, Defect creation by linker fragmentation in metal-organic frameworks and its effects on gas uptake properties. Inorg. Chem. 53 (2014) 6914–6919.

[73] Y. He, J. Shang, Q. Gu, G. Li, J. Li, R. Singh, P. Xiao, P.A. Webley, Converting 3D rigid metal–organic frameworks (MOFs) to 2D flexible networks via ligand exchange for enhanced CO_2/N_2 and CH_4/N_2 separation. Chem. Commun. 51 (2015) 14716–14719.

[74] K. Suzuki, K. Ikari, H. Imai, Synthesis of Silica Nanoparticles Having a Well-Ordered Mesostructure Using a Double Surfactant System. J. Am. Chem. Soc. 126 (2003) 462–463.

[75] J. Kobler, K. Möller, T. Bein, Colloidal Suspensions of Functionalized Mesoporous Silica Nanoparticles. ACS Nano 2 (2008) 791–799.

[76] R. Abazari, A. R. Mahjoub, S. Sanati, Magnetically recoverable Fe_3O_4-ZnO/AOT nanocomposites: Synthesis of a core–shell structure via a novel and mild route for photocatalytic degradation of toxic dyes, J. Mol. Liq. 223 (2016) 1133–1142.

[77] S. Tai, W. Zhang, J. Zhang, G. Luo, Y. Jia, M. Deng, Y. Ling, Facile preparation of UiO-66 nanoparticles with tunable sizes in a continuous flow microreactor and its application in drug delivery. Microporous Mesoporous Mater. 220 (2016) 148–154.

[78] R. Abazari, A. R. Mahjoub, Potential applications of magnetic β-$AgVO_3$/$ZnFe_2O_4$ nanocomposites in dyes, photocatalytic degradation, and catalytic thermal decomposition of ammonium perchlorate. Ind. Eng. Chem. Res. 56 (2017) 623–634.

[79] S. M. Mousavi, A. R. Mahjoub, R. Abazari, Green synthesis of ZnO hollow sphere nanostructures by facile route at room temperature with efficient photocatalytic dye degradation, RSC Adv. 5 (2015) 107378–107388.

[80] F. Fazlali, A. R Mahjoub and R. Abazari, A new route for synthesis of spherical NiO nanoparticles via emulsion nano-reactors with Enhanced Photocatalytic Activity, Solid State Sci. 48 (2015) 263–269.

[81] K. C. Barick, S. Nigam, D. Bahadur, Nanoscale assembly of mesoporous ZnO: A potential drug carrier. J. Mater. Chem. 20 (2010) 6446–6452.

[82] K. Vimala, K. Shanthi, S. Sundarraj, S. Kannan, Synergistic Effect of Chemo-Photothermal for Breast Cancer Therapy Using Folic Acid (FA) modified Zinc Oxide Nanosheet. J. Colloid Interface Sci. 488 (2017) 92–108.

Graphical Abstract